Monitoring and Modeling Drainage Network Contraction and Dry Down in Mediterranean Headwater Catchments

Alfonso Senatore[1], Massimo Micieli[2,1], Alessio Liotti[1], Nicola Durighetto[2], Giuseppe Mendicino[1], Gianluca Botter[2]

[1] Department of Environmental Engineering, University of Calabria, Rende, Cosenza, Italy.

[2] Department of Civil, Environmental and Architectural Engineering, University of Padua, Padua, Italy.

Corresponding author: Alfonso Senatore (alfonso.senatore@unical.it)

Key Points:

- We analyze for the first time the network shrinking and dry down in two seasonally dry Mediterranean headwater catchments
- Accumulated excess precipitation controls the observed variability of network dynamics, with a relevant role of evapotranspiration
- The modeling of the active network spatial patterns based on topographic and geological information achieved accuracies higher than 90%

Abstract

Enhancing an understanding of expansion/contraction dynamics of active drainage networks is fundamental for both scientific purposes and environmental planning and management. This study analyzes for the first time the network shrinking and dry down in two seasonally dry Mediterranean catchments (overall area 1.15 km^2) using a comprehensive approach based on monitoring and modeling of the active network. A seasonal field campaign consisting of 19 subweekly visual surveys was carried out at the beginning of the summer of 2019. Observations were then used to calibrate and validate an integrated model aimed at estimating the time evolution of the total active drainage network length based on meteorological drivers and defining the position of the active stretches based on topographic and geological information. Statistical modeling of the active length showed that weather can successfully describe the observed variability of network dynamics during the summer recession. In particular, the study emphasizes the role of evapotranspiration in the seasonal contraction of the stream network. The modeling of the spatial patterns of the active network achieved good performance when topographic data were used as explanatory variables. Nevertheless, the model performance further increased when site-specific geological information was integrated into the model, with accuracies higher than 90% in cell-by-cell comparisons. The proposed methodology, which combines meteorological, topographic and geological information in a sequential manner, was able to accurately represent the space/time dynamics of the active drainage network in the study area, proving to be an effective and flexible tool for the study of network dynamics.

1 Introduction

Virtually all watercourses experience discontinuous flows along their drainage network. Nonpermanent streams can be observed not only in dry regions but also in most first-order channels (headwaters represent more than 89% of the global river network; Ward et al., 2020), even in wet climates (Tooth, 2000; Larned et al., 2010; Fritz et al., 2013; Datry et al., 2014; Durighetto et al., 2020). Given a potential (geomorphic) river network (i.e., defined as the set of incised channels with banks and a definable channel head; Zimmer and McGlynn, 2017), its temporary portion responds to weather and climate changes at different time scales, from single events to multiyear scales (Costigan et al., 2016), causing spatial and temporal variability of local hydraulic conditions. Such temporary portions of rivers entail stream network expansion, contraction and fragmentation with important implications across many research fields. In particular, stream intermittency is important for freshwater ecology (Datry et al., 2014; Vander Vorste, 2019), biogeochemical cycles (Abbott et al., 2016; Berger et al., 2017; Dupas et al., 2019), carbon dioxide emissions (Schiller et al., 2014; Boodoo et al., 2017; Datry et al., 2018), hydrology (e.g., Godsey and Kirchner, 2014; Jensen et al., 2017; Mendicino and Colosimo, 2019), watershed management and policy (Nikolaidis et al., 2013; Acuña et al., 2014).

Studying temporary rivers is particularly challenging both for ecologists, who need to characterize ‘shifting mosaics’ of lotic, lentic and terrestrial habitats (Datry et al., 2016), and for hydrologists, who address the topic of ‘zero flow’ in developing nonlinear and/or threshold-based approaches (e.g., Zehe and Sivapalan, 2009; Botter et al., 2009; Mendicino and Senatore, 2013a; McInerney et al., 2019). Temporary rivers are also an open issue for/in water policy. For example, dynamic streams are sought to be better integrated into the European Union legislation (Nikolaidis et al., 2013; Reyjol et al., 2014), especially in view of the increasing impact of

climate change and land use development in Mediterranean Europe (Skoulikidis et al., 2017), which are expected to shift permanent streams to temporary (Ward et al., 2020). In the Mediterranean region, stream types with extremely erratic flow regimes exist, identified with specific names ("fiumara" in southern Italy; "wadi" in the Middle East and northern Africa) addressing typical geological, hydrological and ecological traits.

Several pioneering studies of rivers with discontinuous flow were carried out already in the 1960s and 1970s (Gregory & Walling, 1968; Morgan, 1972; Blith & Rodda, 1973; Anderson & Burt, 1978; Day 1978, 1980; Roberts & Archibold, 1978; Gregory & Gardiner, 1979), mainly for specific hydrological purposes (i.e., assessing the link between drainage density and the hydrological response to precipitation). These early studies, however, soon lost their driving force (Godsey and Kirchner, 2014). Recently, the multifaceted implications of river network dynamics have contributed to a renewed interest in the scientific community on temporary streams. Table 1 shows a representative, although not exhaustive, selection of hydrological studies concerning river network dynamics monitoring (and modeling, in several cases) carried out in the last 20 years. Different monitoring approaches were adopted, from relying on stream gauges for long-range analyses (e.g., Costigan et al., 2015) to aerial/satellite images (e.g., Wigington et al., 2005; Phillips et al., 2011). However, given several technical issues (e.g., problems related to zero-flow stream gauge readings, Zimmer et al., 2020; or limits of aerial surveys, Spence & Mengistu, 2016; Tomaštík et al., 2019), the prevailing observation method is represented by visual surveys, always more often aided by water presence sensors (Goulsbra et al., 2014; Pierce and Lindsay, 2015; Assendelft and van Meerveld, 2019; Jensen et al., 2019; Kaplan et al. 2019; Paillex et al., 2020) that can significantly increase the time resolution of the datasets.

Table 1 indicates that very few studies were carried out in temperate Mediterranean climates with cool wet winters and warm dry summers, which promote the seasonality of river regimes. Among them, Godsey and Kirchner (2014) mapped active stream dynamics in four mainly snow-dominated Californian headwater catchments, focusing on the correlation between the active drainage network length and the specific discharge. In the same region (northern California), Lovill et al. (2018) monitored four headwater drainage networks in the early and late summer of different years, highlighting the importance of lithological characteristics for understanding drainage network persistency. However, intraseasonal changes in the active network within Mediterranean climates characterized by higher summer temperatures and an extensive seasonal imbalance between precipitation and evapotranspiration (ET) have not yet been monitored. In these conditions, the climate is expected to exert primary control on flow intermittency and seasonal discharge dynamics (e.g., Medici et al., 2008; Senatore et al., 2011; Garcia et al., 2017). Zimmer and McGlynn (2017) also highlighted that in subtropical climates, there is a direct dependence of seasonality in runoff persistency on ET. Likewise, the mean potential ET was one of the explanatory variables used by Gonzalez-Ferreras and Barquin (2017) in their random forest-based classification model for identifying temporal or perennial river segments.

102 **Table 1.** Intercomparison of recent studies addressing river networks dynamics monitoring.
103

Reference	Location	Climate	Observations	Areal extent	Time extent
Wigington et al., 2005	Agricultural catchments in western Oregon, USA	Cool, wet winters and warm, dry summers, little snowfall	Aerial photographs	5 catchments from 21.6 to 47.8 km^2	Summer 1997, Winter of 1998-99
Malard et al., 2006	Braided glacial river in Switzerland	Alpine	24 field surveys; turbidity measurements	0.67 km^2	Monthly interval, from 1997 to 1999
Doering et al., 2007	River stretch of a river in north-eastern Italy	Mixed Alpine and Mediterranean Mean precipitation 2150 mm $year^{-1}$ Local climate is influenced by both snowmelt and precipitation regimes	Tens of field surveys	Unconstrained 41.5 km river segment	April 2003-October 2004
Jaeger et al., 2007	Forested landscapes in Washington State	Mean precipitation from 2260 to 2800 mm $year^{-1}$	Field mapping of contributing source areas (channel heads)	7 first-order streams with areas from 0.1 to 0.6 km^2	Nine months from February to September
Phillips et al., 2011	Subarctic Precambrian Shield Catchment (Canada)	Mean precipitation about 300 mm $year^{-1}$ Mean January temperature -26.8 °C Mean July temperature 16.8 °C	Multispectral satellite imagery and onsite measurements of storage according to land cover (four surveys)	Three sub-catchments from 8 to 25 km^2	From May to August 2009
Godsey and Kirchner, 2014	Four sites in Sierra Nevada and California Coast Range	Mediterranean, with three out of four sites snow dominated, mean precipitation from 1000 to 1200 mm $year^{-1}$	Field mapping of the stream networks (4 surveys); discharge data available	From 3.6 to 27.2 km^2	Fall 2006, spring and fall 2007 and spring 2008
Goulsbra et al., 2014	Peatland headwater in UK	Mean precipitation 1513 mm $year^{-1}$ Mean monthly temperature 7.0 °C	Network of 40 sensors based on electrical resistance and discharge measures at the outlet	0.43 km^2	Two periods (autumn 2007 and summer 2008), overall almost 4 months
Ågren et al., 2015	Boreal forest	Boreal climate	9 surveys of stream heads of	121 stream heads	2013-2014

	catchment in northern Sweden		the catchment		
Costigan et al., 2015	Tallgrass prairie, Kansas	Temperate Mean precipitation 780 mm year^{-1}	Three headwater stream gages and a downstream gage	Headwater gages: about 1.2 km^2 Downstream gage: 10.6 km^2	25 years
Peirce and Lindsay, 2015	Ephemeral streams in southern Ontario	Mean precipitation 771.4 mm year^{-1} Mean temperature 6.5 °C	56 electrical resistance sensors	Three ephemeral sub-catchments from 0.034 to 0.045 km^2	About 4 months during summer 2011
Shaw, 2016	Forested catchment in central New York State	Humid continental Mean precipitation presumably from 1100 to 1600 mm year^{-1}	Field mapping of flow length (12 surveys); discharge data	1.5 km^2	April-November 2013
Whiting and Godsey, 2016	Headwater streams in Central Idaho	Mean precipitation 700 mm year^{-1}, which primarily falls as snow in wet winter months	3 field surveys per catchment; discharge measurements	4 headwater catchments from 6.5 to 21.4 km^2	Spring and summer 2014
Gonzalez-Ferreras and Barquin, 2017	Catchment in northern Spain draining into the Cantabric Sea	Influence of both temperate oceanic and Mediterranean climate, precipitation over 2000 mm year^{-1} above 1000 m a.s.l.	149 surveys of different river segments over two seasons; aerial images from 2011 to 2014	1200 km^2	Summer 2011 (normal year) and summer 2014 (wet year)
Jensen et al., 2017	Forested headwater catchments in 4 physiographic provinces of the Appalachian Highlands, U.S.	Mean precipitation from 1000 to 1460 mm year^{-1} Mean January temperature from -9 to 3 °C Mean July temperature from 18 to 22 °C	Field mapping of the stream networks (7 surveys); for 8 of the 12 study sites stream flow measurements available	12 headwater catchments with areas from 0.1 to 0.45 km^2 (except one catchment 0.7 km^2 wide)	
Shaw et al., 2017	Birch Creek watershed in the Catskill Mountains of New York State	Humid continental Mean precipitation presumably from 1100 to 1600 mm year^{-1}	Field mapping of flow length; stream gaging	Three catchments from 4.62 to 11.53 km^2	Three surveys on June/July, August, September, October 2014, and November 2015
Zimmer and McGlynn, 2017	Ephemeral-to-intermittent drainage network in the Piedmont region of North Carolina, USA	Subtropical, humid climate Mean precipitation 1136 mm year^{-1} Mean temperature 15.5 °C	77 surface drainage network mapping campaigns over a wide range of runoff magnitudes; runoff and groundwater measurements	0.033 km^2	October 2014 to June 2016
Floriancic et al.,	Alpine catchment,	Alpine	Seven discharge measures in	4 sub-catchments areas	One winter

2018	Switzerland	Mean precipitation 1738 mm year^{-1} Mean temperature 0.2°C	four nested sub-catchments; stream water electrical conductivity and water chemistry	varying from 1.4 km^2 to 5.1 km^2; total area 14.4 km^2	recession period (four months)
Lovill et al., 2018	Northern California Coast Range	Mediterranean, with mean precipitation 2000 mm year^{-1} Mean temperature 13 °C	Field mapping of the stream networks (from 2 to 4 surveys for each watershed); discharge data available	Four catchments from 2.75 to 5.59 km^2 (except one catchment 16.97 km^2 wide)	Two rounds in early and late summer, years 2012, 2014 and 2015
Ward et al., 2018	Headwater mountain catchment in Oregon, USA	Mean precipitation 2302 mm year^{-1} Mean January temperature 0.6°C Mean July temperature 17.8 °C (from Greenland, 1993)	4 field surveys, 15 pressure transducers	0.96 km^2	Field surveys from May to August 2016, pressure transducers: 11 months from October 2015
Jensen et al., 2019	High-relief headwater catchment in southwest Virginia	Mean precipitation over 1000 mm year^{-1} Mean January temperature from -4 to 1 °C Mean July temperature from 19 to 22 °C	51 flow intermittency sensors and field measurements	0.33 km^2	10 months
Kaplan et al., 2019	Various nested sub-catchments in the Attert catchment, Luxembourg	Influence of oceanic climate Mean annual precipitation about 850 mm year^{-1} Maximum temperature of 17 °C in July and minimum of 0 °C in January	time-lapse imagery, electric conductivity and stage measurements (182 sites of observations)	28 km^2 (total catchment area)	Overall, about 4 years from 2013 to 2017
Van Meerveld et al., 2019	Headwater catchment in Switzerland	Alpine Mean precipitation 2300 mm year^{-1}	3 field surveys, streamflow in a neighbouring catchment	0.13 km^2	October and November 2016, August 2018
Durighetto et al., 2020	Rio Valfredda (Piave river basin), northern Italy	Alpine Mean precipitation about 1500 mm year^{-1}	10 field surveys	5.3 km^2	July to early November 2018
Paillex et al., 2020	Val Roseg, Bernina Massif, Swiss Alps	Alpine Mean precipitation about 1000 mm year^{-1}	modified HOBO sensors for 30 tributary streams	About 28 km^2 (inferred)	July to November 2017, December 2017 to June 2018
Perez et al., 2020	Headwater	Humid subtropical climate	23 overland flow detectors	0.0265 km^2	July 2018 to

	catchment in the Peri Lagoon, island of Santa Catarina, Brazil	Mean precipitation about 1700 mm $year^{-1}$ Average temperature varying between 15 °C and 27 °C	(OFDs) and 11 wells	November 2019

104

Linking the active river network length to weather variables is a straightforward and effective way to model its expansion and contraction dynamics. Many recent studies related the network length directly to river discharge or water level (e.g., Doering et al., 2007; Whiting and Godsey, 2016; Shaw et al., 2017; Zimmer and McGlynn, 2017; Ward et al., 2018; Prancevic and Kirchner, 2019). However, streamflow itself is a dependent variable controlled by the meteorological input, and it is often controlled by precipitation patterns at time scales that differ from those relevant for active channel network dynamics (Shaw, 2016; Durighetto et al., 2020). Furthermore, discharge is much less often recorded than precipitation (Fekete and Vörösmarty, 2007; Kim and Sharma, 2019). Among the relatively few studies relating the active drainage network to weather and climatic drivers (Goulsbra et al., 2014; Ward et al., 2018; Jensen et al., 2018, 2019; Jaeger et al., 2019), Durighetto et al. (2020) were the first to explore the dependence of the active stream length on the aggregation time scale of the underlying meteorological drivers. In the study of Durighetto et al. (2020), the impact of ET on network dynamics was determined to be negligible because of the wet climate characterizing their study area (annual rainfall > 1500 mm). To date, the extent to which this site-specific result can be extended to drier climate settings remains unknown.

A comprehensive modeling framework should associate the estimated active drainage network length to the spatial allocation of flowing river reaches. This procedure is not trivial because the spatial distribution of the active network is arguably dependent on several topographic and geological features. While Biswal and Marani (2010) linked stream network recession features to morphological characteristics, other authors highlighted the importance of subsurface and groundwater processes for the study of spatial patterns of flow persistence (e.g., Godsey and Kirchner, 2014; Goulsbra et al., 2014; Shaw, 2016; Zimmer and McGlynn, 2017; Ward et al., 2018). Jaeger et al. (2007) did not find satisfactory area-slope relationships to explain observed channel head locations in forested landscapes in Northwestern USA. In the same vein, Payn et al. (2012) suggested a decreasing influence of topography on stream base flow contributions during the recession. Floriancic et al. (2018) found large differences in flow rates from neighboring slopes with similar geomorphological features, highlighting the importance of bedrock properties and even of debris cover on space-time variability of contributions to low flows.

In the literature, there are many examples of studies that, though acknowledging that topography does not fully explain the observed spatial variability of the active river network persistency, use topographic and morphologic indices to model network expansion and contraction. Shaw et al. (2017) found statistically significant differences in the mean topographic wetness index (Beven and Kirkby, 1979), hereafter TWI, between ephemeral and perennial channels. Both Gonzalez-Ferreras and Barquin (2017) and Jaeger et al. (2019) included several topographic variables in their sets of independent variables for random forest-based classifications of river network persistency. Jensen et al. (2018) developed logistic regression models of river network dynamics based on terrain metrics and runoff observations. They found that TWI and, to a lesser extent, other topographic indices (e.g., the topographic position index TPI; Guisan et al., 1999) were fundamental parameters for modeling headwater stream network dynamics. Additional field campaigns that exploited water presence sensors confirmed the significant correlation between flow duration and topographic indices such as TWI, TPI or upslope accumulated area in a small catchment in Northeastern USA (Jensen et al., 2019). Existing approaches, however, exploit local morphometric properties of the contributing

catchment and operate at the single-grid pixel or river segment level. Therefore, the dynamics of the whole stream network emerge from the aggregation of the local model results through a bottom-up approach. This can induce significant misestimations of the total active length in some circumstances (Jensen et al., 2018). Moreover, in the existing literature, the effect of stationary topographic and geological characteristics is superimposed on that induced by dynamical hydrometeorological variables, as spatial and temporal patterns of flowing streams are concurrently analyzed via regression models. The influence of topographic and geological attributes on the spatial patterns of flow persistency has not yet been isolated, and the impact of prioritization schemes that involve specific morphometric and geologic characteristics on the ensuing model performance remains unknown.

In this paper, a comprehensive investigation of the recession dynamics of two temporary headwaters in a Mediterranean watershed is presented. The research consists of the following three main steps: 1) field monitoring and visual inspection of the active stream network, characterized by higher than weekly resolution surveys (average time interval of approximately 4-5 days) over a total area > 1 km^2, from the end of the 2019 rainy season (i.e., April) until the complete drying up of the channels (June); 2) statistical modeling of the total active drainage network length by explicitly accounting for the time variability of the hydroclimatic forcing and evapotranspiration dynamics; and 3) prediction of the spatial distribution of the active nodes based on topographic and geological characteristics of the drainage basin.

The application of the proposed novel methodology serves to fulfill the following specific objectives: i) further increasing the range of experimental studies that address temporary streams to characterize the effect of seasonal flow recession on the active channels of a headwater catchment with a temperate (hot-summer) Mediterranean climate; ii) highlighting the time scales of network contraction and seasonal dry down, relating them to relevant climatic variables and evaluating the role of ET in the network contraction; and iii) assessing to what extent the spatial distribution of the active river reaches can be explained by a model relying only on topography and evaluating the model's improvement with additional information related to the geology of the sites.

2 Data and Methods

2.1 Study area and geological setting

The study area consists of two headwater catchments (located approximately at 39.524° N, 16.130° E) feeding the upper course of the Turbolo creek, a tributary of the Crati River in southern Italy (Figure 1a). The Turbolo creek has been investigated for over 20 years (e.g., Mendicino and Sole, 1997; Mendicino, 1999), and its upper course is conventionally closed at the outlet of Fitterizzi, where both a weather station and a water stage gauge are installed, managed by the Regional Agency for the Protection of the Environment (ARPACal).

The upper Turbolo creek catchment is approximately 7 km^2 wide, with elevation ranging from 183 to 1005 m a.s.l. Its channel network mainly consists of two forks, originating from the Calabrian Coastal Range, and is dominated by strongly altered and fractured crystalline-metamorphic rocks that entail widespread slope instability and overall high permeability (Tortorici et al., 1995). Such conditions allow relevant groundwater storage leading to almost perennial flow at the Fitterizzi gauge.

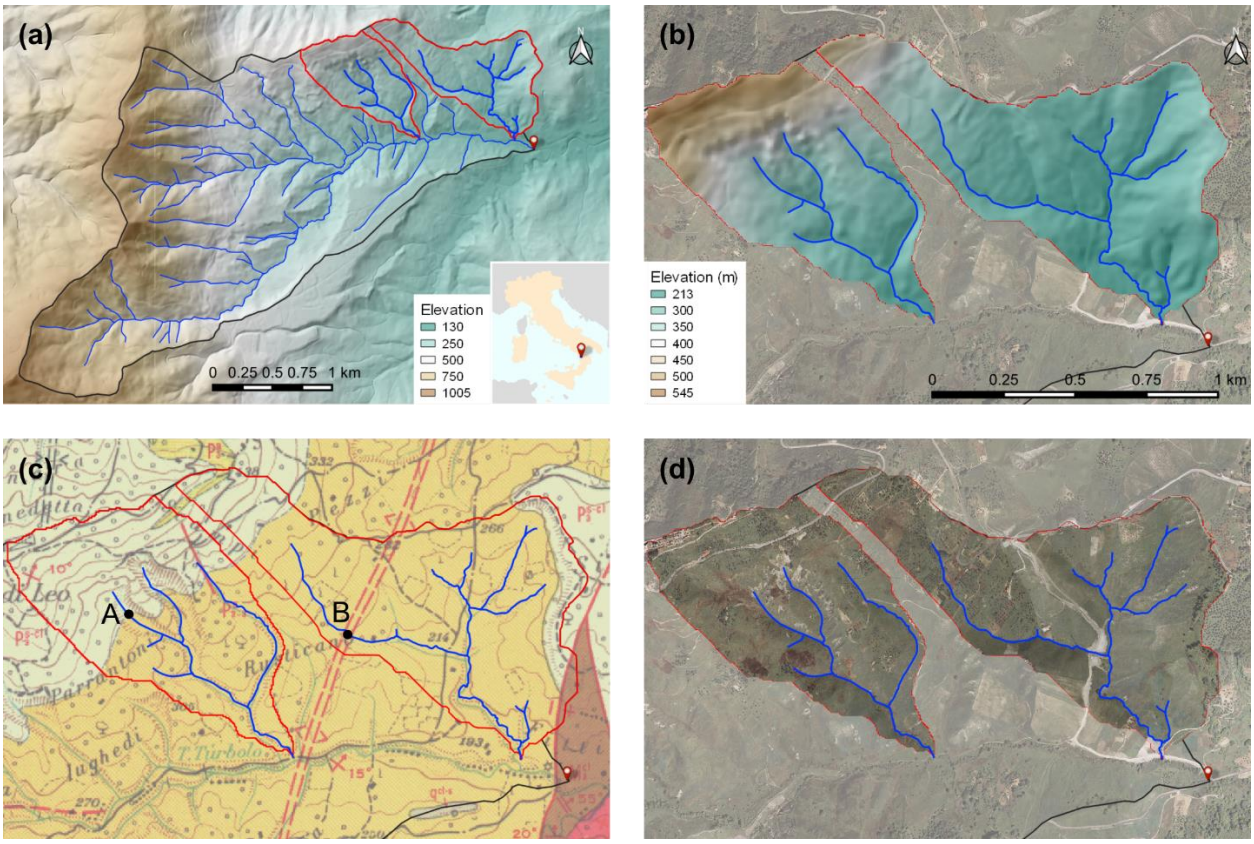

Figure 1. Study area: (a) the Turbolo catchment closed at the Fitterizzi outlet (red pin). Red contours highlight the two headwater catchments analyzed; (b) zoom on the two headwater catchments (W catchment on the left, E catchment on the right); (c) geolithological map of the study area: silty marly clays of the Middle-Late Pliocene are drawn in yellow; overlapping Late Pliocene sandy-conglomerate formations are drawn in light beige. The double dashed red line represents the anticline fold. Point A highlights the intersection at the lowest elevation of the separation line between the two sandy and clay lithological formations with the main channel of the W catchment drainage network, point B the intersection of the anticline fold with the E catchment drainage network; (d) study catchments areas and drainage networks overlaid on orthophotos provided by the Calabria Region geoportal.

The geomorphology of the catchment is characterized by steep slopes on the west side, modeled on the metamorphic rocks. In the eastern part, where the two test catchments fall, slopes are less steep, but very affected by water erosion processes, inducing shallow landslides and soil creep phenomena.

The two headwater catchments selected for this study, hereafter referred to as east/E and west/W catchments (in agreement with their geographical position in Figure 1b), are 0.67 and 0.48 km^2 wide, respectively; their main topographic and geomorphological features are summarized in Table 2. Their dominant lithologies (Figure 1c) are silty marly clays of the Middle-Late Pliocene, with poor erosion resistance and low permeability. North-westerly, poorly consolidated and highly permeable sandy-conglomerate formations of the Late Pliocene (Calabrian) overlap. The sharp contrast of permeability between the two lithologies generates

shallow unconfined aquifers feeding temporary springs. The surface layers of the clay formations are also generally altered and more permeable than the underlying layers. Moreover, they are characterized by variable thicknesses due to the aforementioned geomorphological characteristics and because of an anticline fold, linked to the tectonic processes affecting the entire area (Figure 1c). These layers also contain shallow aquifers seasonally contributing to surface flows.

The surface erosive processes affecting the two test catchments are mainly dominated by surface flowing waters and landslides, which can cause landscape evolution, especially in areas with limited vegetation cover (including agricultural areas). Therefore, the catchment morphology is subject to changes with consequent variations in channel incision and geometry. The W catchment's drainage network is frequently characterized by eroded gullies, steeper morphology and bare surfaces with evident signs of recurrent landslides. On the other hand, the E catchment has gentler slopes. As a comparison, Table 2 shows that the TPI standard deviation is equal to 0.24 and 0.16, respectively, for the W and E catchments. Another important difference between the study sites concerns land use: less than 15% of the W catchment is used for agriculture, while approximately 90% of the E catchment is used for agriculture and pasture (Figure 1d).

Finally, it is noteworthy that stretches with standing water, due to low infiltration rates and morphological irregularities, are not uncommon in the study area. Standing water was not considered as part of the active network, yet it facilitates ephemeral stream reactivations (even of a few hours) in the gullies, even following low rainfall amounts.

2.2 Hydrometeorological dataset

The monitoring station of Fitterizzi (Figure 1a) is very close to the two test catchments (approximately 175 m from the outlet of the E catchment, and approximately 2150 m from the farthest point of the W catchment), therefore it is highly representative of the climate and weather conditions of the test area. The weather data analyzed during the 18-year long period from July 2001 to June 2019 reveal a typical Mediterranean climate (Csa, according to Köppen classification; Köppen, 1936), with hot and dry summers (average July temperature of 24.9 °C) and wet, not very cold winters (average January temperature of 7.9 °C). The average annual precipitation and reference crop evapotranspiration are equal to 1244.7 mm $year^{-1}$ (only 26% of which falls from April to September) and 1235.9 mm $year^{-1}$, respectively (Figures 2a and 2b). The one-year period from July 2018 to June 2019 (corresponding to the dry down month in our survey) was less rainy than average (990.4 mm $year^{-1}$) and evapotranspiration was slightly lower than average (1205.3 mm $year^{-1}$). Nevertheless, May 2019, which is the month with the highest number of field surveys used for this study, was particularly wet (94.6 mm, the second rainiest month in the series).

The total amount of rainfall during the study period (from April 18, 2019 until the end of June 2019) was 101.8 mm, and the corresponding reference evapotranspiration was 375.4 mm (Figure 2c). During this 74-day period, 23 rainy days (precipitation $\geq$ 0.2 mm/d) were observed (18 of which were in May), with the highest intensity of 28.8 mm d^{-1} on May 6. The average number of consecutive dry days was 6.4, but June was almost completely dry. The limited rainfall amounts observed in June corresponded to an almost simultaneous sudden increase in temperatures. Specifically, from June 3 to 7, there was an increase of more than 10 °C in the maximum daily temperature and approximately 8 °C in the mean daily temperature.

Table 2. Summary of the main properties of the E and W catchments and field surveys. GDNL is the geomorphic drainage network length, ADNL the active drainage network length, TWI the topographic wetness index and TPI the topographic position index (calculated through the homonymous GDAL - geospatial data abstraction library - algorithm in QGIS).

Main topographic and geomorphological features			Field surveys			
	E catchment	W catchment	E catchment		W catchment	
Catchment area (km^2)	0.67	0.48	Date	ADNL (km)	Date	ADNL (km)
Maximum altitude (m a.s.l.)	481	545	18 Apr 2019	2.74	18 May 2019	1.33
Mean altitude (m a.s.l.)	263	358	03 May 2019	1.95	21 May 2019	1.20
Minimum altitude (m a.s.l.)	183	213	07 May 2019	2.54	24 May 2019	0.88
Average exposure	NW	NW	11 May 2019	1.95	01 Jun 2019	0.87
Average slope	15°	23°	17 May 2019	2.10	05 Jun 2019	0.45
Maximum TWI	16.21	14.67	21 May 2019	1.68	07 Jun 2019	0.28
Mean TWI	5.13	4.5	24 May 2019	1.62	10 Jun 2019	0.14
Maximum TPI	0.9	2.80	01 Jun 2019	1.40	15 Jun 2019	0.00
TPI standard deviation	0.16	0.24	05 Jun 2019	1.40		
Minimum TPI	-0.93	-1.70	07 Jun 2019	0.15		
GDNL (km)	2.88	2.26	10 Jun 2019	0.00		

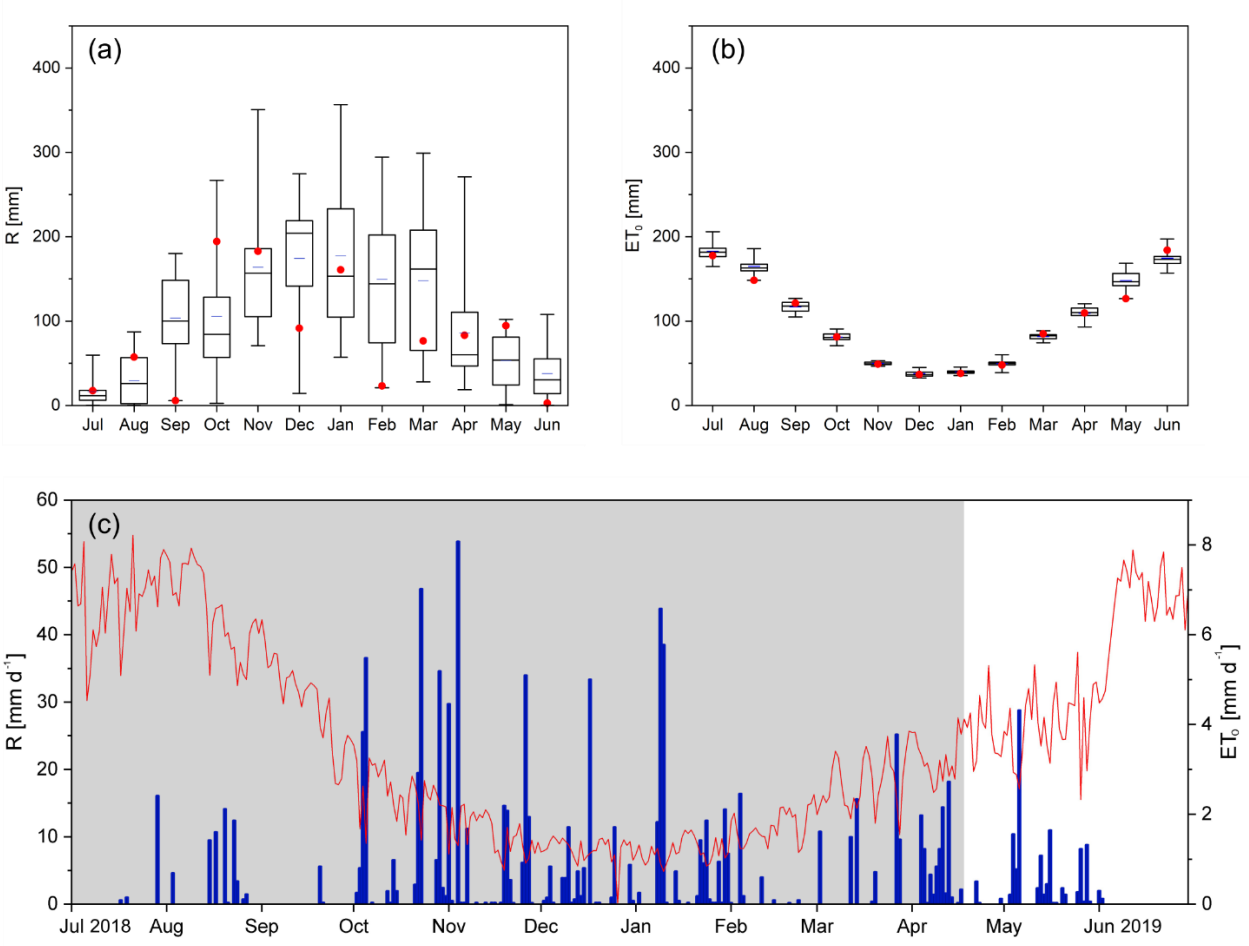

Figure 2. (a) Box plots of accumulated monthly precipitation from July 2001 to June 2019. Blue horizontal lines represent the average values, red dots the values in the period July 2018 – June 2019; (b) same as that of (a), but reference crop evapotranspiration ET_0; (c) time series of daily precipitation and ET_0 in the period July 2018 – June 2019. White background highlights the study period. Note that, while ET_0 in figure (c) was calculated through the Penman-Monteith equation (Allen et al., 1998), due to the numerous gaps in many variables, the monthly ET_0 in figure (b) was calculated through the Hargreaves-Samani equation that was improved following the approach of Mendicino and Senatore (2013b).

Correspondingly, the mean reference evapotranspiration increased from 4.0±0.7 mm d^{-1} during the period of April 18 – June 3 to 6.9±0.6 mm d^{-1} during the period of June 4 – 30.

Water stage data were also available at Fitterizzi. For that outlet, the stage-discharge rating curve was reconstructed by carrying out frequent discharge measurements (approximately one per month) from March to August 2019 with a three-dimensional flow tracker based on the acoustic Doppler velocimeter (ADV) technology, whose sensor allowed reliable measurements starting from flow depths greater than 25 mm, with a maximum tolerance of ±8 mm. From April 18 to June 30, 2019, an almost constant decrease in the average daily discharge was recorded,

from 0.104 m^3s^{-1} to 0.023 m^3s^{-1}, respectively. The highest average daily discharge (0.198 m^3s^{-1}) was recorded after the event that occurred on May 6.

2.3 Field surveys and drainage network mapping

The on-site surveys, aimed at reconstructing the topology and dynamics of the flowing network, were carried out from April 2019 until complete dry down occurred in June 2019. The mapping strategy that was replicated was defined by Durighetto et al. (2020) and consisted of hiking the whole catchments, moving upstream along the reaches and collecting the coordinates and activity status of each network node, aided by a geotracking device. The average distance between neighboring nodes was set as 20 m; however, in some cases, adverse morphological and vegetation conditions (especially in the W catchment) did not allow a uniform distance value to be maintained throughout the network. Each node was classified as active when there was flowing water on it and dry otherwise (dry node or node with standing water). The minimum width of the flowing water for identifying an active node was fixed to 10 cm, in line with Durighetto et al. (2020).

A total of 11 (8) complete surveys were carried out for the E (W) catchment, until the complete dry down of the whole network in both catchments took place (Table 2). Afterward, periodic (e.g., biweekly) inspections were carried out during the summer season to verify the lack of surface flows in the test catchments (the reactivation of the network took place in November 2019). The overall duration of the campaigns was 53 and 28 days, respectively, for the E and W catchment. For the E catchment, the average time interval between two consecutive surveys was 5.3 days (maximum 15 days, minimum 2 days); for the W catchment, it was 4 days (maximum 8 days, minimum 2 days). Surveys were performed under different weather conditions.

On-field recorded information was archived in a GIS environment in which the nodes were connected and the whole network was delineated for each survey carried out. Specifically, the drainage networks were reconstructed from a combination of information derived from on-field surveys and official sources, such as the digital terrain model (DTM) and orthophotos provided by the Calabria Region geoportal. The DTM has a spatial resolution of 5 m (enough to reconstruct accurate stream networks; Li and Wong, 2010) and was preliminarily corrected with a pit removal algorithm to eliminate the most evident DTM artifacts (i.e., pits collecting drainage from more than 4 cells, i.e., 100 m^2), and then flow directions and flow accumulation were calculated through a classical D8-type algorithm (Jenson and Domingue, 1988). The consistency of the flow directions derived from the DTM with the observations was checked by overlaying the tracked nodes. Inconsistencies were solved by manually modifying the DTM, but differences in positioning were never greater than two cells (i.e., < 10 m). The surveyed nodes were connected by stretches following the GIS-derived flow accumulation grids, and from each grid cell in between two observed nodes, a virtual node was extracted. Each stretch was then set as active only if both the upstream and downstream nodes were observed as active.

Subsequently, for each survey, every node was assigned with an active/nonactive label that made it possible to calculate some global properties, such as the total active drainage network length (ADNL [km]) and the active drainage density (ADD [km^{-1}]). Furthermore, the persistency of active drainage on each stretch *i* during the survey period was quantified through a persistency index P_i calculated as the ratio of the number of surveys with the stretch classified as active to the total number of surveys (Durighetto et al., 2020).

2.4 Modeling the drainage network length dynamics

The models used for estimating the total active streamflow network length follow the approach adopted by Durighetto et al. (2020), but some novel elements have been introduced to represent the peculiarity of the climate in the study area and the seasonality of the flow regime.

In the first model (model 1, hereafter), the ADNL is assumed as linearly dependent on the antecedent excess precipitation EP_T (mm) accumulated during T days:

$$ADNL(t) = k_{EP} \cdot EP_T(t) \cdot H[EP_T(t)] \quad (1)$$

where H is the Heaviside step function and k_{EP} (km mm^{-1}) is a parameter representing the rate of $ADNL$ increase per unit of EP_T. EP_T is calculated integrating the daily excess precipitation EP (mm d^{-1}) over the period T:

$$EP_T(t) = \int_{t-T}^{t} EP(\tau)d\tau \quad (2)$$

where $EP(t) = R(t) - ET_C(t)$, with R (mm d^{-1}) as the daily precipitation and ET_C (mm d^{-1}) as the daily crop evapotranspiration. The latter can be calculated following Allen et al. (1998) using a crop coefficient k_c:

$$ET_C = k_c \cdot ET_0 \quad (3)$$

where ET_0 is the daily reference crop evapotranspiration estimated with data provided by the Fitterizzi monitoring station. It is noted that the daily excess precipitation is forced to be positive or null.

The calibration of the model relies on the parameters k_c, k_{EP} and T. By fixing the values of k_c and T, linear regression was used to estimate k_{EP}, and the coefficient of determination R^2 was calculated. The parameters k_c and T were estimated by maximizing R^2 by searching in a two-dimensional domain in which physically reasonable ranges of (0, 1) and (0, 60 days) were assumed for k_c and T, respectively. Calibrations were performed for both the E and W catchments, checking their robustness through leave-one-out cross-validations. Furthermore, each study catchment was used for the validation of the model parameters found during the calibration in the other catchment.

Model 1 is the only model of the three models proposed by Durighetto et al. (2020) that accounts for evapotranspirative processes. In contrast to the alpine climate where it was first applied, in our study area, the advent of high temperatures, typically from late spring, leads to a significant and rather sudden increase in evapotranspiration (Figure 2c), making occasional rain showers ineffective for the recharge of groundwater. Therefore, the term EP_T tends to zero rather rapidly (depending on T), resulting in the complete dry down of the stream network. Notably, in the calibration strategy adopted in this paper, the parameter k_c represents the average behavior of

the whole vegetation in the catchment, and it can implicitly include the effect of water stress conditions; therefore, the accumulated ET_C calculated along the whole analysis period is presumably representative of the accumulated actual evapotranspiration.

The importance of evapotranspiration for the contraction and dry down of the Turbolo river network was further evaluated by comparing model 1 to the other two models proposed by Durighetto et al. (2020) in which *EP* is replaced by precipitation. Specifically, the simplest of these models simply assumes that the *ADNL* linearly depends on the precipitation R_T (mm) accumulated in the previous T days through a coefficient k_P (km mm^{-1}). It will be called model 2, hereafter:

$$ADNL = k_P \cdot R_T(t) \tag{4}$$

The last model (model 3, hereafter) considers two amounts of precipitation (R_{T1} and R_{T2}) as explanatory variables for *ADNL*, accumulated over different periods T_1 and T_2 to account for different contributions (surface and subsurface/groundwater, respectively) to the flow generation processes. These two quantities are then linked to *ADNL* with linear regression using the coefficients k_{P1} and k_{P2}:

$$ADNL = k_{P1} \cdot R_{T_1}(t) + k_{P2} \cdot R_{T_2}(t) \tag{5}$$

Similar to model 1, models 2 and 3 also have no parameters accounting for the length of the permanent drainage network. Therefore, model 2 needs calibration only for parameters k_P and T, while k_{P1}, k_{P2}, T_1 and T_2 are calibrated for model 3. The calibration procedures adopted for these two models are similar to that used with model 1, i.e., for each model, the set of parameters maximizing R^2 was selected (for further details, the reader is referred to Durighetto et al., 2020). The performance indices adopted for model comparisons were the R^2 and the mean absolute error (*MAE*) between the observed and modeled ADNLs.

2.5 Modeling the spatial distribution of the active drainage network

Compared to other approaches found in the literature that are aimed at providing spatially distributed information of the degree of network activity (e.g., Gonzalez-Ferreras and Barquin, 2017; Jensen et al., 2018; Jaeger et al., 2019), the novelty of the method herein proposed is that it starts from the active drainage network total length (whose extent is estimated based on meteorological variables in a dynamic manner), and then focuses on the allocation of the estimated total length in the space, depending on local geomorphological and/or geological features. The latter step is carried out by transferring the information concerning the nodes surveyed to the grid cells making up the DTM, thus representing the study area through a regular grid with a resolution equal to that of the DTM.

A straightforward and objective method for assessing the spatial distribution of the *ADNL* consists of relying on topographic features. Among the various terrain metrics, the TWI is likely the one that more clearly shows a direct link with the runoff persistency (e.g., Shaw et al., 2017; Jensen et al., 2018; 2019).

If it is assumed that the persistency of surface runoff in a given grid cell is directly dependent on the TWI, then it is possible to spatially distribute the active network objectively. This can be accomplished by locating it such that it starts from the cell with the highest TWI value and gradually decreases until it reaches a threshold value that corresponds to a network length equal to the (observed or modeled) ADNL. This approach can be pursued once a bijective correspondence between network length and TWI values has been defined. Specifically:

- if two grid cells are connected horizontally (i.e., in the N-S or E-W directions), the associated length of the channel is equal to the lateral dimension (resolution) of the cell l;
- if two grid cells are connected diagonally (NW-SE or NE-SW directions), the associated length is equal to $\sqrt{2}\cdot l$;
- in the case of isolated cells, the associated length can be arbitrarily assumed between 0 and $\sqrt{2}\cdot l$ (in our case, a length equal to $0.5\cdot l$ was set).

However, the presence of pedological and lithogeological singularities can weaken the hypothesis of the dependence of the active network location only on topography (e.g., Godsey and Kirchner, 2014), especially during the recession phase (Payn et al., 2012) and even in neighboring catchments with similar geomorphological characteristics (Floriancic et al., 2018). In such cases, the general rule of dependence on higher TWI values can be amended by prioritizing/penalizing reaches that have specific features (e.g., the presence of a spring or, conversely, a wide alluvial bed with high storage potential). In particular, if permanent or semipermanent springs are identified, active cells can be allocated primarily downstream of the springs, still following a higher-TWI-based rule that is limited to the downstream channels until the outlet is reached and then moving to the remaining portion of the drainage network. Of course, this approach cannot be separated from an accurate knowledge of the pedolithology and bedrock geology of the study area.

The accuracy of the model was evaluated through cell-by-cell comparisons involving, for every survey i, all the cells of the geomorphic drainage network. The results were summarized in confusion matrices, from which an accuracy index was achieved:

$$Accuracy_i = \frac{TP_i + TN_i}{n} \quad (6)$$

where TP_i and TN_i represent the cells correctly modeled as active (true positives) and not active (true negative), respectively, and n is the total number of cells belonging to the geomorphic drainage network, i.e., the sum of TP_i, TN_i, false positives FP_i (i.e., cells erroneously modeled as active) and false negatives FN_i (i.e., cells erroneously modeled as not active).

3 Results

3.1 Active drainage network observations

Table 2 shows the observed ADNL for the 19 surveys carried out in the study area. In the E catchment, the ADNL ranged from a maximum of 2.74 km (95% of the potential -geomorphic-drainage network, ADD = 4.09 km^{-1}) to 0 in approximately 53 days, with an average observed value of approximately 1.59 km. The high initial value of the active network length is most likely

due to the precipitation events in the previous two weeks (approximately 80 mm and 13 rainy days out of 14; Figure 2c). Despite a general decreasing trend, the dynamics of the ADNL are nonmonotonic because the rainfall events between the 3rd and 7th of May (45.8 mm overall) and between the 11th and 17th of May (25 mm overall) led to a temporary increase of the variable. On the other hand, in the W catchment after the first survey (18th of May) no relevant rainfall events occurred until the complete dry down (approximately 28 days later), with an average of less than 1 mm d^{-1} of rainfall; hence, we observed a continuous decrease of ADNL from the first observed value (1.33 km, corresponding to 59% of the geomorphic drainage network, and an ADD = 2.77 km^{-1}) to 0, with an average observed ADNL of approximately 0.64 km.

Disconnected ADNL (i.e., the length of the portion of the active drainage network not connected to the outlet) was not particularly relevant in both catchments. In the E catchment, only during one survey (Jun 7) was the active network disconnected (5.3% of the geomorphic network length). On the other hand, the rougher morphology of the W catchment allowed identifying some disconnected portions of the network in 6 out of 8 surveys, but with disconnected lengths that never exceeded 15% of the geomorphic network.

Figure 3 shows the spatial distribution of the persistency index P_i in the study catchments. Owing to the ephemeral nature of the stream network in this region, the mean persistency values in the E and W catchments are 0.55 and 0.30, respectively. Figure 3 also highlights a significant spatial variability of P throughout the network; in particular, both catchments have one main branch where P_i values are remarkably higher than all the other reaches. This pattern can be reasonably linked to the lithogeological features of the study sites (Section 2.1). Specifically, point A (reported in both Figures 1c and 3) upstream of the most persistent branch in the W catchment represents the lowest elevation intersection of the separation line between the two sandy and clay lithological formations with the main channel, while point B (also drawn in Figures 1c and 3) upstream of the most persistent branch in the E catchment highlights the approximate location of the intersection of the anticline fold with the drainage network. Both points A and B play an important role because the geological features that correspond to those points foster temporary springs.

3.2 Active drainage network length modeling

Figure 4 relates the ADNLs of the E and W catchments to the average daily discharge Q at the Fitterizzi gauge. The observed discharge is likely to smooth the actual relationship between the active drainage network and the runoff produced by the test catchments since Q reflects the hydrological processes taking place in a larger area (7 km^2 against 1.15 km^2), including the mountain areas with geolithological characteristics leading to semiperennial flow (Section 2.1). Nevertheless, in both catchments, we tried to express the observed ADNLs as a function of the observed discharge as:

$$ADNL = \alpha \cdot (Q - Q_0)^{\beta} \quad (7)$$

where α is a constant, β is the scaling exponent and Q_0 is the highest discharge value for which ADNL = 0. Calibration led to a value of 0.494 for the scaling exponent value in the E catchment, which is within the literature range (Godsey and Kirchner, 2014; Jensen et al., 2017).

Instead, in the W catchment, it is >1 (Figure 4b). This difference in the exponents is possibly generated by the difference in the dates when the surveys started (in the W catchment, the surveys started closer to the dry down than in the E catchment).

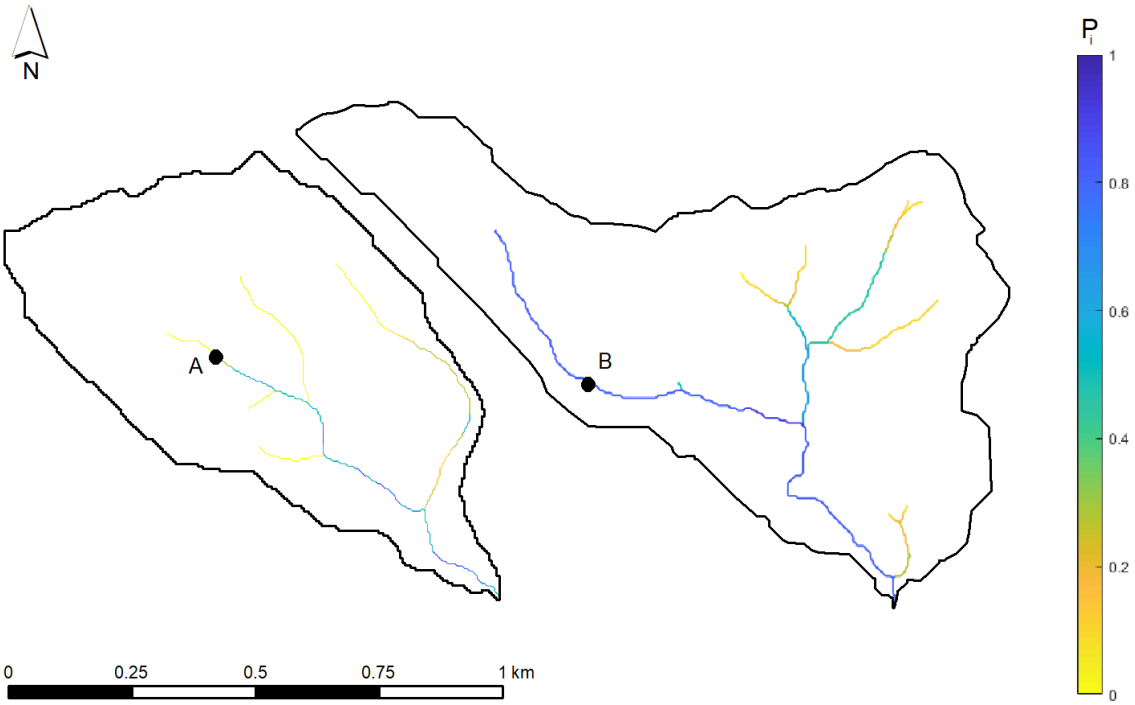

Figure 3. Persistency index P_i for the E and W catchments. Points (A) and (B) from Figure 1c are also reported.

The power regressions based on Equation 7 were well correlated to observed ADNLs (R^2 equal to 0.87 and 0.94, *MAE* equal to 0.23 km and 0.08 km, respectively, for the E and W catchment). Nevertheless, they oversimplify the different response times of different hydrological processes (i.e., active network expansion/contraction and discharge generation/routing) triggered by common climatic forcing, enhancing the risk of spurious correlations. In Figures 4a and 4b, the colors of the circles and the red dashed tracks highlight the time evolution of observed points in the *Q*-ADNL domain. In the E catchment, we observed some signals of the counterclockwise hysteretic effect described by Zimmer and McGlynn (2017) during the precipitation event that took place on May 6, 2019. The ADNL was slightly lower during the rising limb than during the receding limb (ADNL = 1.948 km and Q = 0.066 m^3s^{-1} on May 3, ADNL = 1.953 km and Q = 0.064 m^3s^{-1} on May 11), confirming that network contraction might have a delayed response compared to flow recession. Other examples in support of this finding exist. For instance, in the E catchment, despite a flow recession of approximately 0.012 m^3s^{-1} from the 1st to the 5th of June (with 2.8 mm of rainfall in-between), ADNL did not vary. The counterclockwise hysteretic effect emerges despite that the size of the catchments where the ADNL was monitored is much smaller than the contributing area at the discharge gauging station. Instead, such an instance is expected to smooth the discharge response and hasten the ADNL response.

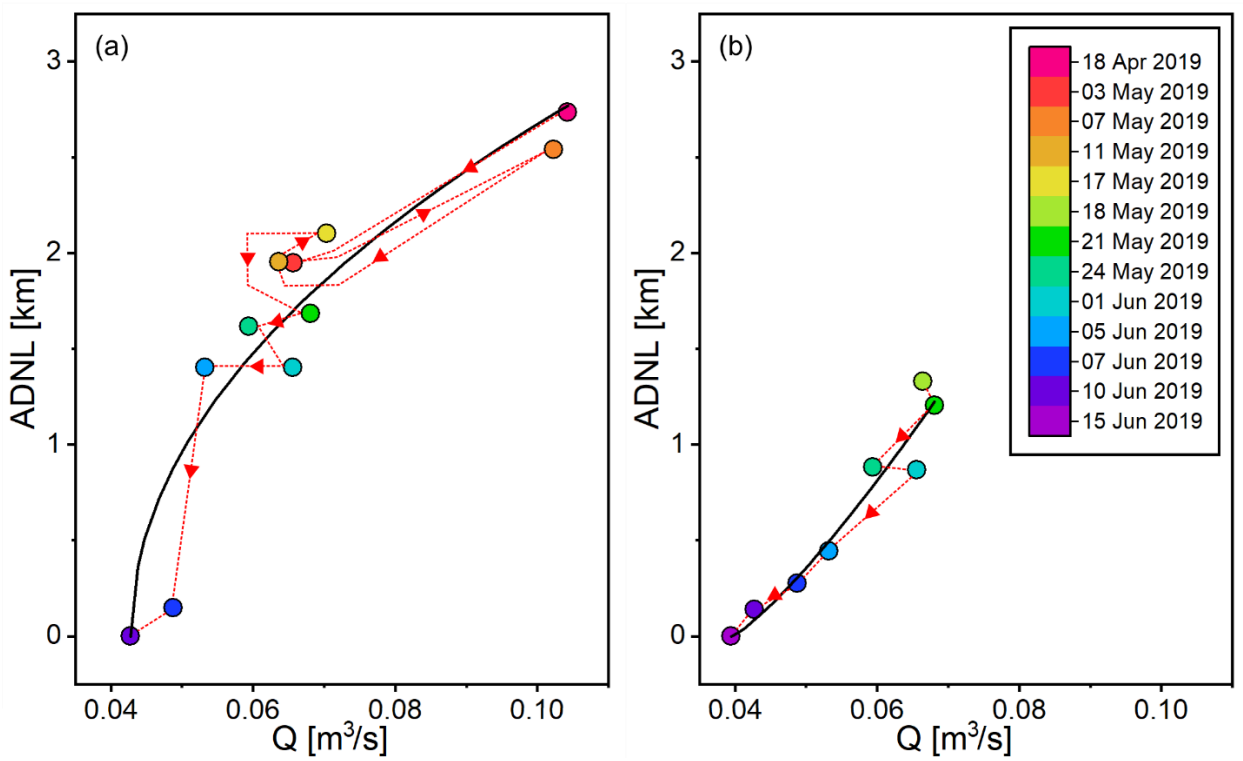

Figure 4. Observed mean daily runoff Q versus ADNL observed in (a) the E and (b) the W catchment. Different fill colors highlight the measuring date for each point of the series, while the red dashed tracks indicate the time evolution of observations in the Q-ADNL domain.

Drainage network dynamics were then related to the underlying meteorological drivers (precipitation and evapotranspiration) using the statistical models described in Section 2.4. Table 3 summarizes the results achieved using model 1 that accounts for evapotranspiration, and its performance is compared to models 2 and 3 that only rely on precipitation data.

As per the best performing model (model 1), we observed some differences in the calibrated parameters between the E and W catchments (Table 3). The period T over which the excess precipitation was accumulated on the E catchment was slightly shorter than the W catchment (31 vs. 34 days). This result can be explained by the smoother landscape of the E catchment compared to the W catchment, where incised channels might strongly connect the surface drainage network to the subsurface flow. The calibrated k_c value in the E catchment was also lower than the optimal k_c in the W catchment (0.449 vs. 0.755), in line with the observed differences in the land use of the two catchments (with more agriculture and controlled vegetation growth in the E catchment). The patterns of the R^2 values in the T-k_c domain for both the E and the W catchments are shown in Figures 5a and 5b, respectively. Even though R^2 values tend to be higher in the W catchment, which can be simulated more 'easily' (fewer surveys and monotonic descending behaviors of the ADNL), the patterns are quite similar in the two cases and suggest that the drainage network dynamics in our case studies cannot be explained by the short-term (i.e., few days) trend of weather variables.

536 **Table 3**. Comparison of the calibrated parameters with models 1, 2 and 3 and related performance. The left side of the table refers to
537 the calibration performed in the E catchment, where R^2 and the mean absolute error (*MAE*) for the W catchment were calculated using
538 the mean values of the parameters k_{EP}, k_P, k_{P1} and k_{P2}. Analogously, the right side of the table shows the results achieved with the
539 calibration performed in the W catchment. Parameters units: T, T_1, T_2 [days]; k_c [-]; k_{EP}, k_P, k_{P1} and k_{P2} [km mm^{-1}]; R^2 [-]; *MAE* [km].
540

Model	Parameters (E catchment calibration)	E catchment (calibration)		W catchment (validation)		Parameters (W catchment calibration)	E catchment (validation)		W catchment (calibration)	
		R^2	*MAE*	R^2	*MAE*		R^2	*MAE*	R^2	*MAE*
Model 1 Eq. (1)	T = 31 k_c = 0.449 k_{EP} = 0.034±0.0006	0.92	0.19±0.02	0.83	0.43	T = 34 k_c = 0.755 k_{EP} = 0.035±0.0003	0.79	0.53	0.98	0.05±0.01
Model 2 Eq. (4)	T = 24 k_P = 0.026±0.0007 T_1 = 5	0.63	0.42±0.03	0.83	0.70	T = 9 k_P = 0.047±0.0012 T_1 = 8	0.58	0.58	0.96	0.07±0.01
Model 3 Eq. (5)	T_2 = 24 k_{P1} = 0.025±0.0023 k_{P2} = 0.021±0.0009	0.78	0.27±0.02	0.95	0.59	T_2 = 18 k_{P1} = 0.029±0.0015 k_{P2} = 0.007±0.0005	0.58	0.70	0.99	0.04±0.01

541

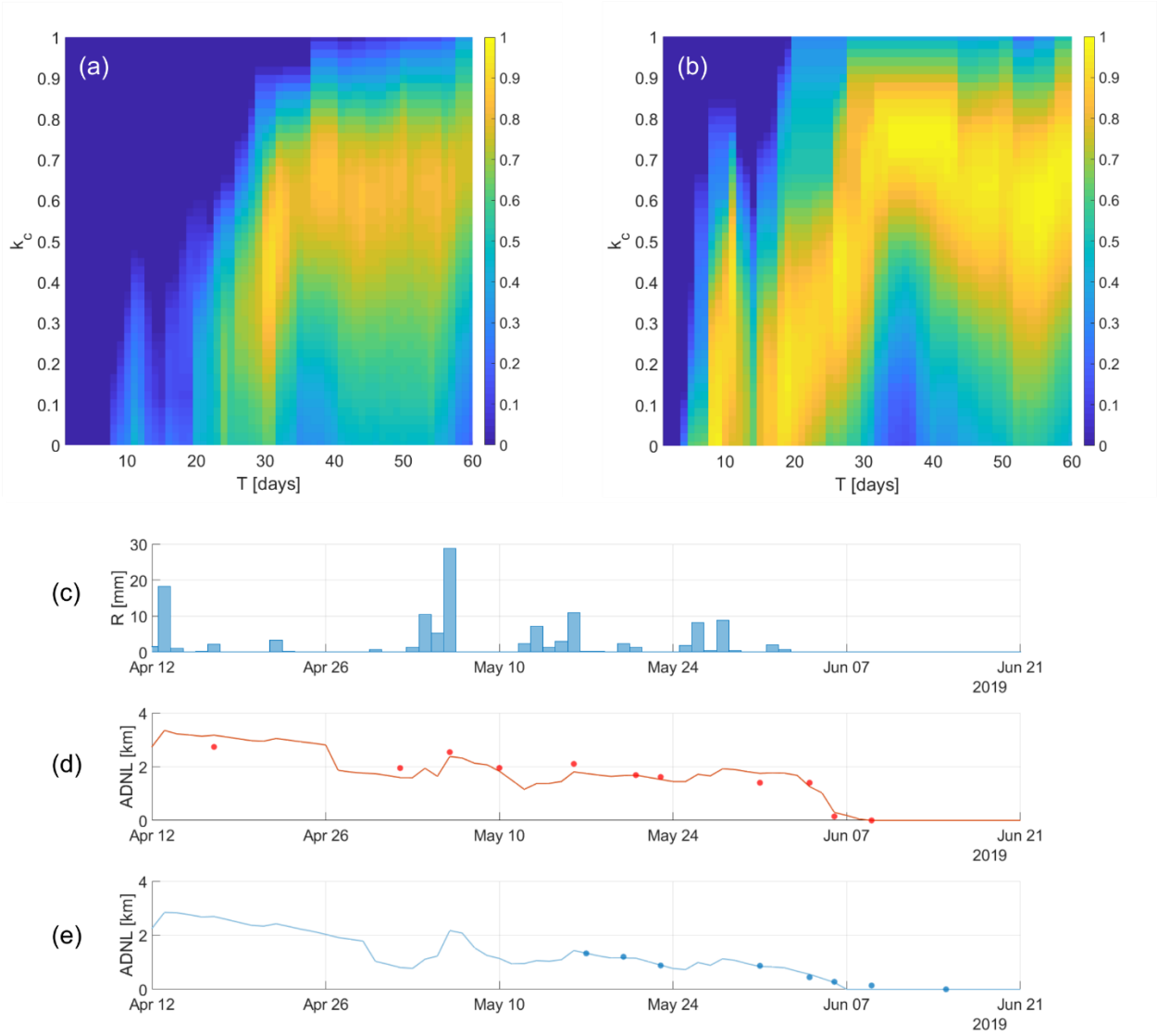

Figure 5. (a) R^2 of model 1 as a function of T and k_c, calibrated over the observations in the E catchment; (a) R^2 of model 1 as a function of T and k_c, calibrated over the observations in the W catchment; (c) daily precipitation during the period from April 12 to June 21, 2019; (d) calibrated model based on model 1 in the E catchment (red points represent the observed ADNL values); (e) calibrated model based on model 1 in the W catchment (blue points represent the observed ADNL values).

The T and k_c parameters summarize the effects of the differences in topography and land cover in the two catchments. Taking this into account, interestingly, the ratio between the ADNL and the accumulated excess precipitation is almost the same (0.034±0.0006 and 0.035±0.0003 for the E and W catchment, respectively). The cross-validation analysis highlighted the robustness of the model (coefficients of variation on the order of 0.01) that was also confirmed by the *MAE* values achieved with different parameter subsets.

Figure 5c shows the modeled network dynamics using the parameter sets calibrated with both the test catchments and the observations. The graph provides a visual representation of the

good performances of the models that are confirmed by the high R^2 and low *MAE* values (Table 3). Model 1 not only performs very well in the catchment where it is calibrated (R^2 = 0.92 and 0.98, *MAE* = 0.19±0.02 km and 0.05±0.01 km, for the E and W catchments, respectively) but also provides reliable forecasts in the corresponding validation catchments (R^2 = 0.83 and *MAE* = 0.43 km in the W catchment; R^2 = 0.79 and *MAE* = 0.53 km in the E catchment). The decrease of performance observed when evapotranspiration is not included in the statistical regression (models 2 and 3) indicates that in Mediterranean climates, *ET* plays a critical role for drainage network dynamics. Furthermore, the physical explanation of the difference between the calibrated parameters of models 2 and 3 in the two catchments is less straightforward.

3.3 Spatial distribution of the active drainage network

According to the proposed approach (Section 2.5), the first step for modeling the spatial distribution of the active drainage network consists in finding, for each of the test catchments, a relationship that allows one to calculate the drainage network length for predefined TWI threshold values. Figure 6 shows the variation of the active network length, considering as active only the cells of the DTM having TWI values equal to or greater than a given threshold. To facilitate the comparison between the two catchments, the active network length and the TWI were scaled with the catchment area (ADD) and the maximum TWI value (TWI_{max}), respectively. The graph highlights an almost linear increase in ADD while reducing the TWI threshold in the W catchment; in the E catchment, instead, the increase in ADD is slower for higher TWI values (i.e., at lower elevations) and faster for lower values. Figure 6 resembles the right tails of TWI frequency distributions in the study catchments (corresponding to the channelized network). Moreover, the observed pattern of ADD vs. TWI/TWI_{max} in the E catchment reflects the higher bifurcation ratio of the upstream network, and the presence of a single relatively long main channel that dominates the landscape in the lower part of the basin. Therefore, in the E catchment, the ADNL is more (less) sensitive to changes in the TWI threshold for lower (higher) TWI values.

The TWI-ADNL relationship can be used for modeling the spatial distribution of the active network if TWI values of the cells are significantly correlated with the corresponding persistency values. Specifically, it can be hypothesized that a cell in the channel network with higher TWI is active for longer than a cell with a smaller TWI; hence, its persistency P_i is higher. Indirectly, this assumption implies that the activation of the reaches in the whole network follows a hierarchical order since TWI is a time-invariant feature.

TWI values in the cells that host the geomorphic channel networks are well correlated with P_i (Figure 7) both in the E catchment (r = 0.714, $p << 0.001$) and the W catchment (r = 0.833, $p << 0.001$). Correlation analysis suggests that other topographic indices such as TPI, which proved to be useful in other contexts (e.g., Jensen et al., 2018), cannot add significant information in this case (r = 0.059 and 0.098, for the E and W catchments, respectively).

The ADNL-TWI relationships found in the two test catchments were used to drive the spatial distribution of the modeled ADNL in the cells of the DTM. Figures 8a and 8b (left histogram series, labeled with “T”) summarize the performance of the whole modeling chain (i.e., ADNL modeling based on effective rainfall and consequent spatial allocation of the channelized sites), highlighting for each survey in each catchment, the percentage of *TP*, *TN*, *FP* and *FN*. The mean accuracy in the E catchment (Figure 8a) varies from 72.8% (June 1) to 99.4% (June 10), with an average value of 81.7%. In the W catchment (Figure 8b), the accuracy varies

from 84.8% (June 7) to 97.6% (June 15), with an average value of 89.5%. *FP* and *FN* percentages are comparable in both catchments (*FP* = 7.8% and *FN* = 10.5% in the E catchment, *FP* = 4.2% and *FN* = 6.3% in the W catchment), highlighting the similar model performance in the two case studies.

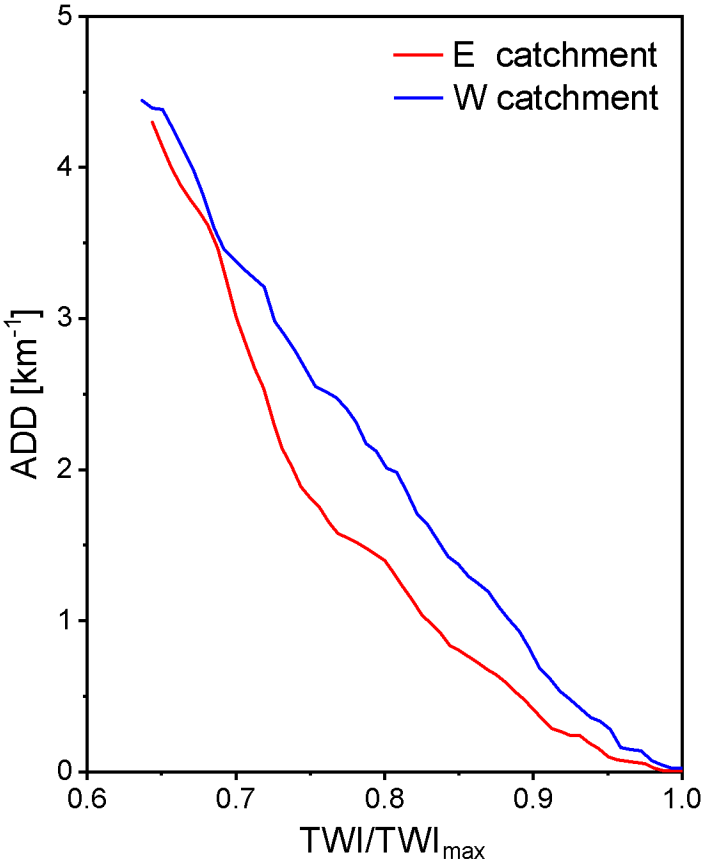

Figure 6. Relationship between the ADD obtained when only the cells of the DTM having the ratio TWI/TWI$_{max}$ equal to or greater than a given threshold are activated and the respective TWI/TWI$_{max}$ thresholds.

A comparison of the modeled spatial distribution of the active cells with the observational data (some examples representative of different wetness conditions are given in Figure 9) highlighted that model performance can be further improved integrating the topographical features summarized by the TWI with lithogeological information. Specifically, the stretches intersecting points A (sand-clay interface, Figure 1c) and B (anticline) where temporary springs emerge (Section 3.1) need to be prioritized while defining the activation rules since observations showed that cells belonging to such stretches are more prone to activation than cells with higher TWI values belonging to other stretches. Therefore, the spatial allocation of the active cells in each catchment is ruled by two TWI-ADNL curves, with the second (low priority) activated only when the maximum ADNL associated with the first (high priority – stretch intersecting point A or B) is reached.

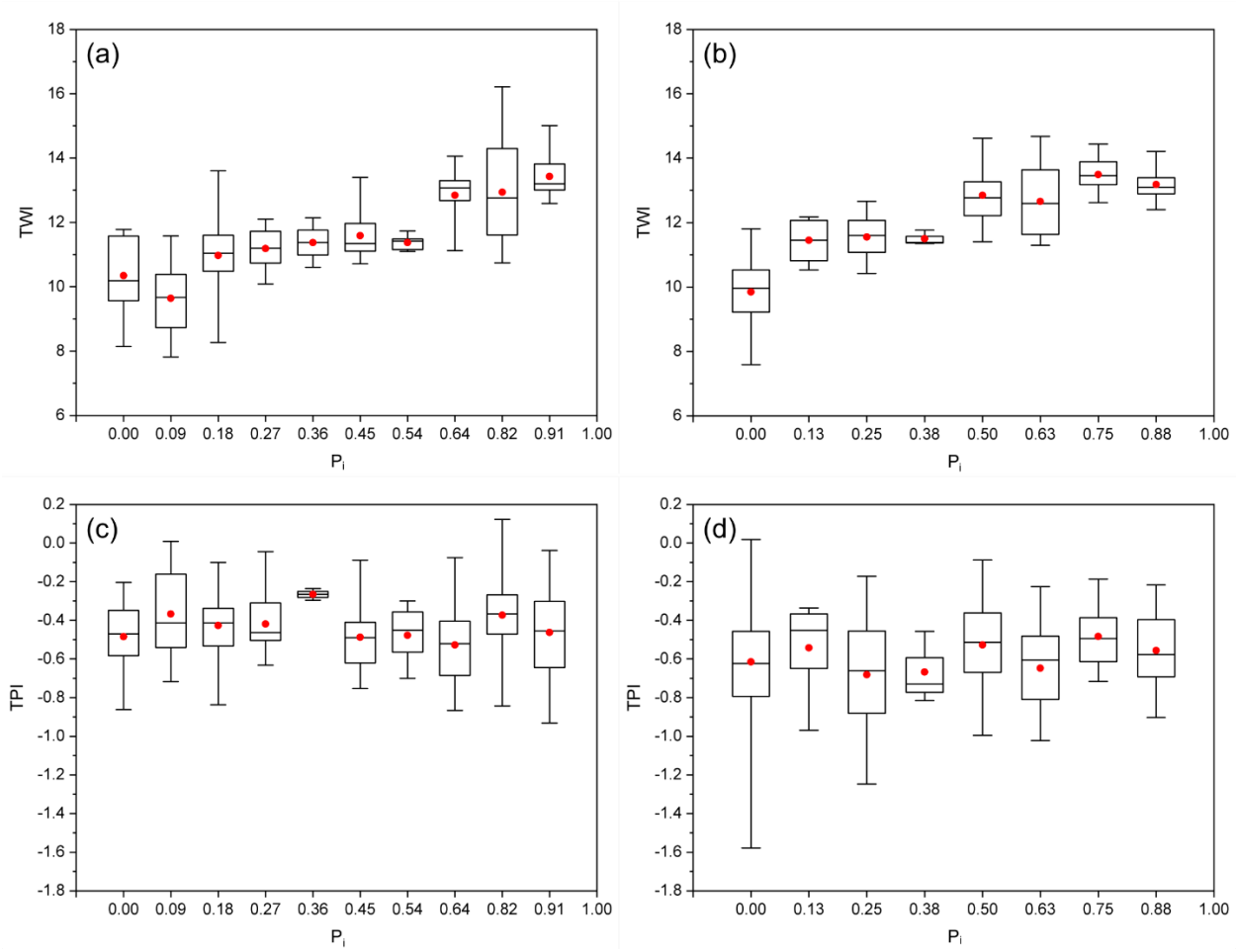

Figure 7. Box plots of (a) TWI distribution in the E catchment, (b) TWI distribution in the W catchment, (c) TPI distribution in the E catchment, (d) TPI distribution in the W catchment, divided according to the corresponding P_i values, for each DTM cell belonging to the geomorphic drainage network.

Assuming the priorities suggested by the analysis of the lithogeological features, the results shown in Figures 8a and 8b (right histogram series, labeled with "T-G") were achieved. The mean accuracy in the E catchment increases by 9.4% compared to the model relying only on TWI (Figure 8a), with an average value of 91.0% and a range that varies from 84.9% (June 7) to 99.4% (June 10). In the W catchment (Figure 8b), the improved version of the model increases model performances to a lesser extent (+ 2.4%). *FP* and *FN* percentages remain comparable in both catchments, but with smaller values compared to the version of the model that exploits only topographic information (*FP* = 3.2% and *FN* = 5.8% in the E catchment, *FP* = 3.1% and *FN* = 5.0% in the W catchment).

Figure 9 shows some examples of the cell-by-cell comparisons between observed and modeled active drainage networks using both the TWI-based model and the integrated topographical and lithogeological model. Specifically for the E catchment, the surveys performed on May 7 and June 5 were selected as representative of wet and dry (but without

complete dry down) conditions, respectively. On the first date (Figure 9a), the catchment was quite wet and the prioritization of the stretch intersecting the anticline had a small effect on the observed spatial pattern of the active network. On the other hand, on June 5 (Figure 9b), the same strategy led to an improvement in the total accuracy of more than 20%. Concerning the W catchment, the example reported in Figure 9c, which refers to June 1, highlights the beneficial consequences implied by the prioritization of the main channel (with an improvement in the accuracy of almost 11%); however, when the main channel is not fully active (June 5, Figure 9d), the two approaches are almost equivalent.

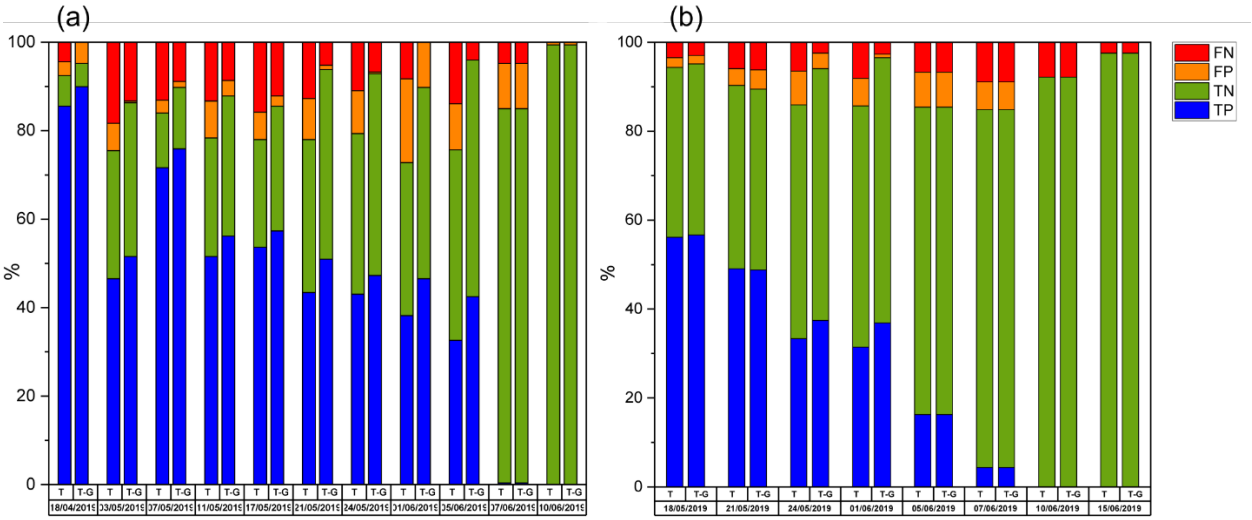

Figure 8. Summary of cell-by-cell comparison of the observed and modeled spatial distribution of active cells for all surveys: (a) E catchment; (b) W catchment. In each graph, the left histogram series are related to the model using only TWI (label "T"), the right histogram series to the model using both TWI and lithogeological information (label "T-G"). *TP*: True Positives; *TN*: True Negatives; *FP*: False Positives; *FN*: False Negatives.

4 Discussion and Conclusions

This study presents the results of a comprehensive analysis based on a seasonal field campaign in two Mediterranean catchments in which the active network was monitored during the flow recession phase occurring at the beginning of the summer of 2019 until complete dry down. The paper also presents an integrated model of the space/time dynamics of the active drainage network that couples meteorological, topographic and geological information in a sequential manner. The temperate Mediterranean climate of the study area (typically characterized by hot and dry summers) jointly with the specific focus on network dry down represents one of the key novelties of this work, which expands the range of hydroclimatic settings within which empirical information on the temporal dynamics of the actively flowing streams is available.

The results shown in this paper concur to strengthen the hypothesis that the temporal variability of the overall active network length is modulated by weather dynamics. Specifically, the high correlation between the antecedent excess precipitation and the active network length suggests the following major conclusions: (i) *ADNL* temporal variability can be successfully described based on weather drivers; (ii) in the analyzed meteorological setting, accounting for

evapotranspiration is essential to explain the observed dynamics of the active streams; and (iii) while the temporal dynamics of the ADNL are controlled by the underlying climatic variability, the actual length of active streams does depend on topographic and/or geological features, which in model 1, influence the period of integration T over which the accumulated excess precipitation is evaluated (longer in the more incised but smaller W catchment, shorter in the gentler E catchment). Provided that differences in land cover (which modulates evapotranspiration) and topography are summarized by the different values of the parameters k_c (Equation 3) and T (Equation 1), the two neighboring study catchments show almost the same proportionality factor between accumulated excess precipitation and *ADNL* (i.e., ≈ 0.035 km mm^{-1}), despite the underlying differences in catchment area and geomorphic drainage density.

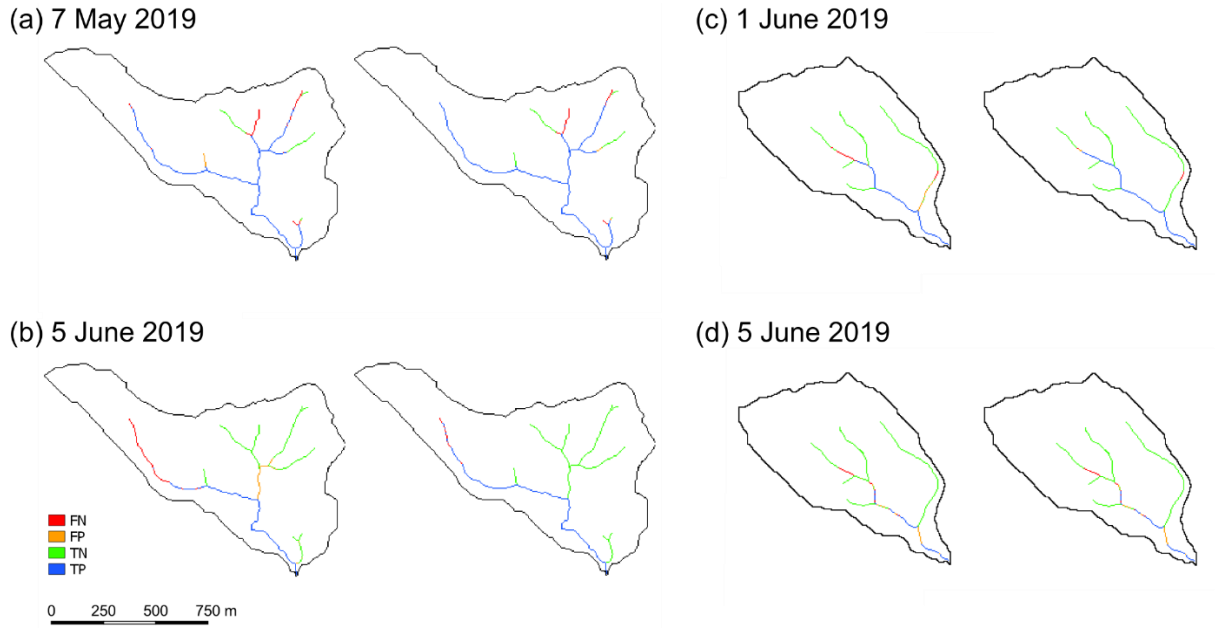

Figure 9. Cell-by-cell comparison of the observed and modeled spatial distribution of active cells: (a) E catchment, May 7, 2019; (b) E catchment, June 5, 2019; (c) W catchment, June 1, 2019; (d) W catchment, June 5, 2019. For each figure in the panel, the left map is related to the model using only TWI, the right map to the model using both TWI and lithogeological information.

The statistical model linking active length and antecedent excess precipitation was compared to an alternative approach that relies on a power function linking *ADNL* and discharge, widely used for various field applications. Our results indicate (Section 3.2) a good performance of the discharge power function (Equation 7) in describing *ADNL* dynamics, though the performance was slightly lower than that of model 1. Beyond the performance the models, we argue that relying on weather variables rather than water discharge for modeling *ADNL* dynamics is preferable for three reasons: first, discharge and active network length are two different types of responses to a common hydrological forcing, even though these responses are characterized by distinct characteristic lag-times. This feature is highlighted by the counterclockwise hysteretic behavior observed between Q and ADNL (Shaw, 2016; Zimmer and McGlynn, 2017), which implies that the discharge response is faster than the active network

length; second, in many settings, discharge data are much rarer and much more challenging to gather than weather data; third, the use of antecedent meteorological data makes the parameters of the regression less sensitive to the specific observation period during which the survey was carried out. Indeed, Table 3 shows that model 1 calibrated in the W catchment provides reasonable results also in the E catchment, while the power function calibrated in the W catchment with the scaling exponent greater than 1 is not applicable in the E catchment.

While the weather forcing controls the observed temporal changes in the active network length, the main drivers of the active network's spatial patterns are represented by physiographic features such as topography, hydraulic properties of surface soil, bedrock structure and geological singularities such as faults and anticlines in line with previous studies (Goulsbra et al., 2014; Godsey and Kirchner, 2014; Costigan et al., 2016, Whiting and Godsey, 2016; Jensen et al., 2018, 2019; Prancevic and Kirchner, 2019). Specifically, the high correlation between P_i and TWI found in both catchments, which is here enhanced by the spatial homogeneity of soil properties, confirms the primary importance of morphometric features in delineating spatial patterns of active drainage networks (Jensen et al., 2018).

The relatively low number of disconnections observed in the study sites can be explained by the prevalence of clay soils that do not promote the formation of losing streams and water reinfiltration processes. Nevertheless, even in a rather homogenous geological setting such as that characterizing the study area (Figure 2c), topography cannot fully explain the spatial dynamics of stream expansions and contractions (Jensen et al., 2019). In our case study, accounting for some key geological features (namely, the sand-clay interface and the anticline) helped to improve the representation of the spatial patterns of active stream dynamics.

The proposed approach based on a bijective correspondence between the network length and TWI (either with or without prioritization) was shown to be effective and flexible. In general, the concept of prioritization proposed in this work can be made more complicated; e.g., the priority given to the stretches located downstream of a geological singularity can be effective only within a given region of influence, e.g., as defined by a certain TWI (lower) threshold. However, the adoption of this strategy is conditioned by a detailed knowledge of the specific features of the catchment under investigation and can be hardly generalized.

Whether the spatial patterns of the expansion/contraction process are regulated only by topographical characteristics or by a combination of morphologic and geolithological characteristics, the dependence of the persistency on time-invariant features of the catchment evidenced by our data supports the hypothesis of the existence of a predefined hierarchical order in the activation/deactivation of stretches, as proposed by Botter and Durighetto (2020).

Future work will expand the analysis of the network dynamics in the study area beyond the recession phase, including the winter reactivation phase. As suggested by previous studies (e.g., Zimmer and McGlynn, 2018), the expansion and contraction of the flowing network are deeply connected to the seasonal variations of the underlying shallow unconfined aquifers. Given the peculiar geological features of the area, the temporary springs are likely to reactivate only when the water table elevation exceeds a given threshold according to a nonlinear process. This hypothesis will be evaluated in future studies that also use a higher-resolution DTM derived from a LiDAR survey, UAV-based monitoring and more detailed information about soil properties and bedrock structure.

Acknowledgments, Samples, and Data

We thank Pasqualino Artiglieri and Licio Argento for their help in performing the field surveys and Francesco Colosimo and Roberto Di Gaudio for their support with discharge measurements. We thank the "Centro Funzionale Multirischi" of the Calabrian Regional Agency for the Protection of the Environment for providing the observed meteorological dataset.

This study was supported by the European Research Council (ERC) DyNET project funded through the European Community's Horizon 2020 - Excellent Science - Programme (grant agreement H2020-EU.1.1.-770999).

Weather data are delivered, upon request, by the "Centro Funzionale Multirischi – ARPACAL" (http://www.cfd.calabria.it/). The original DTM, the geolithological map of the study area and the orthophotos are provided by the Calabria Region geoportal: http://geoportale.regione.calabria.it/opendata. The modified DTM and the experimental data collected for this study are available at Senatore et al. (2020).

References

Abbott, B. W., Baranov, V., Mendoza-Lera, C., Nikolakopoulou, M., Harjung, A., Kolbe, T., et al. (2016). Using multi-tracer inference to move beyond single-catchment ecohydrology. Earth Sci. Rev. 160, 19–42. doi: 10.1016/j.earscirev.2016.06.014.

Acuña, V., Datry, T., Marshall, J., Barceló, D., Dahm, C. N., Ginebreda, A., ... & Palmer, M. A. (2014). Why should we care about temporary waterways?. Science, 343(6175), 1080-1081. DOI: 10.1126/science.1246666.

Ågren, A. M., Lidberg, W., & Ring, E. (2015). Mapping temporal dynamics in a forest stream network—implications for riparian forest management. Forests, 6(9), 2982-3001. https://doi.org/10.3390/f6092982.

Allen, R. G., Pereira, L. S., Raes, D., & Smith, M. (1998). Crop evapotranspiration-Guidelines for computing crop water requirements-FAO Irrigation and drainage paper 56. Fao, Rome, 300(9), D05109. http://www.scscourt.org/complexcivil/105CV049053/volume3/172618e_5xAGWAx8.pdf

Anderson, M. G., & Burt, T. P. (1978). Analysis of spatial water quality and stream networks in the southern Cotswolds during and after the drought of 1976. Earth Surface Processes, 3(1), 59-69. doi:10.1002/esp.3290030106.

Assendelft, R. S., & van Meerveld, H. J. (2019). A Low-Cost, Multi-Sensor System to Monitor Temporary Stream Dynamics in Mountainous Headwater Catchments. Sensors, 19(21), 4645. https://doi.org/10.3390/s19214645.

Berger, E., Haase, P., Kuemmerlen, M., Leps, M., Schaefer, R., & Sundermann, A. (2017). Water quality variables and pollution sources shaping stream macroinvertebrate communities. Science of the Total Environment, 587, 1–10. https://doi.org/10.1016/j.scitotenv.2017.02.031.

Beven, K. J., & Kirkby, M. J. (1979). A physically based, variable contributing area model of basin hydrology/Un modèle à base physique de zone d'appel variable de l'hydrologie du

784 bassin versant. Hydrological Sciences Journal, 24(1), 43-69.
785 https://doi.org/10.1080/02626667909491834.

786 Biswal, B., & Marani, M. (2010). Geomorphological origin of recession curves. Geophysical
787 Research Letters, 37(24). https://doi.org/10.1029/2010GL045415.

788 Blyth, K., & Rodda, J. (1973). A stream length study. Water Resources Research, 9(5), 1464–
789 1461.

790 Boodoo, K. S., Trauth, N., Schmidt, C., Schelker, J., & Battin, T. J. (2017). Gravel bars are sites
791 of increased CO2 outgassing in stream corridors. Scientific Reports, 7(1), 1–9.
792 https://doi.org/10.1038/s41598-017-14439-0.

793 Botter, G., Porporato, A., Rodriguez-Iturbe, I., & Rinaldo, A. (2009). Nonlinear storage-
794 discharge relations and catchment streamflow regimes. Water Resources Research,
795 45(10), W10427. https://doi.org/10.1029/2008WR007658.

796 Costigan, K. H., Daniels, M. D., & Dodds, W. K. (2015). Fundamental spatial and temporal
797 disconnections in the hydrology of an intermittent prairie headwater network. Journal of
798 Hydrology, 522, 305-316. https://doi.org/10.1016/j.jhydrol.2014.12.031.

799 Costigan, K. H., Jaeger, K. L., Goss, C. W., Fritz, K. M., & Goebel, P. C. (2016). Understanding
800 controls on flow permanence in intermittent rivers to aid ecological research: integrating
801 meteorology, geology and land cover. Ecohydrology, 9(7), 1141-1153.
802 https://doi.org/10.1002/eco.1712.

803 Day, D. (1978). Drainage density changes during rainfall. Earth Surface Processes, 3, 319–326.
804 https://doi.org/10.1002/esp.3290030310.

805 Day, D. (1980). Lithologic controls of drainage density: a study of six small rural catchments in
806 New England, N.S.W. Catena, 7, 339-351. https://doi.org/10.1016/S0341-
807 8162(80)80024-5.

808 Datry, T., Larned, S. T., & Tockner, K. (2014). Intermittent rivers: A challenge for freshwater
809 ecology. Bioscience, 229–235. https://doi.org/10.1093/biosci/bit027.

810 Datry, T., Pella, H., Leigh, C., Bonada, N., & Hugueny, B. (2016). A landscape approach to
811 advance intermittent river ecology. Freshwater Biology, 61(8), 1200-1213.
812 https://doi.org/10.1111/fwb.12645.

813 Datry, T., Foulquier, A., Corti, R., Von Schiller, D., Tockner, K., Mendoza-Lera, C., ... &
814 Gücker, B. (2018). A global analysis of terrestrial plant litter dynamics in non-perennial
815 waterways. Nature Geoscience, 11(7), 497-503. https://doi.org/10.1038/s41561-018-
816 0134-4.

817 Doering, M., Uehlinger, U., Rotach, A., Schlaepfer, D. R., & Tockner, K. (2007). Ecosystem
818 expansion and contraction dynamics along a large Alpine alluvial corridor (Tagliamento
819 River, Northeast Italy). Earth Surface Processes and Landforms: The Journal of the
820 British Geomorphological Research Group, 32(11), 1693-1704.
821 https://doi.org/10.1002/esp.1594.

822 Dupas, R., Abbott, B., Minaudo, C., & Fovet, O. (2019). Distribution of landscale units within
823 catchments influences nutrient export dynamics. Frontiers in Environmental Science, 7,
824 43. https://doi.org/10.3389/fenvs.2019.00043.

Durighetto, N., Vingiani, F., Bertassello, L. E., Camporese, M., & Botter, G. (2020). Intraseasonal Drainage Network Dynamics in a Headwater Catchment of the Italian Alps. Water Resources Research, 56(4), e2019WR025563. https://doi.org/10.1029/2019WR025563.

Fekete, B. M., & Vörösmarty, C. J. (2007). The current status of global river discharge monitoring and potential new technologies complementing traditional discharge measurements. IAHS publ, 309, 129-136. http://hydrologie.org/redbooks/a309/309015.pdf.

Floriancic, M. G., van Meerveld, I., Smoorenburg, M., Margreth, M., Naef, F., Kirchner, J. W., & Molnar, P. (2018). Spatio-temporal variability in contributions to low flows in the high Alpine Poschiavino catchment. Hydrological processes, 32(26), 3938-3953. https://doi.org/10.1002/hyp.13302.

Fritz, K. M., Hagenbuch, E., D'Amico, E., Reif, M., Wigington Jr, P. J., Leibowitz, S. G., ... & Nadeau, T. L. (2013). Comparing the extent and permanence of headwater streams from two field surveys to values from hydrographic databases and maps. JAWRA Journal of the American Water Resources Association, 49(4), 867-882. https://doi.org/10.1111/jawr.12040.

Garcia, C., Amengual, A., Homar, V., & Zamora, A. (2017). Losing water in temporary streams on a Mediterranean island: Effects of climate and land-cover changes. Global and Planetary Change, 148, 139-152. https://doi.org/10.1016/j.gloplacha.2016.11.010.

Godsey, S., & Kirchner, J. (2014). Dynamic, discontinuous stream networks: Hydrologically driven variations in active drainage density, flowing channels and stream order. Hydrological Processes, 28, 5791–5803. https://doi.org/10.1002/hyp.10310.

González-Ferreras, A. M., & Barquín, J. (2017). Mapping the temporary and perennial character of whole river networks. Water Resources Research, 53(8), 6709-6724. https://doi.org/10.1002/2017WR020390.

Goulsbra, C., Evans, M., & Lindsay, J. (2014). Temporary streams in a peatland catchment: pattern, timing, and controls on stream network expansion and contraction. Earth Surface Processes and Landforms, 39(6), 790-803. https://doi.org/10.1002/esp.3533.

Gregory, K., & Walling, D. (1968). The variation of drainage density within a catchment. International Association of Scientific Hydrology Bulletin, 13, 61–68. https://doi.org/10.1080/02626666809493583.

Gregory, K., & Gardiner,V. (1979). Comment on drainage density and streamflow: Acloser look by S. L. Dingman.Water Resources Research, 15(6), 1662–1664. https://doi.org/10.1029/WR015i006p01662.

Guisan, A., Weiss, S. B., & Weiss, A. D. (1999). GLM versus CCA spatial modeling of plant species distribution. Plant Ecology, 143(1), 107-122. https://doi.org/10.1023/A:1009841519580.

Jaeger, K. L., Montgomery, D. R., & Bolton, S. M. (2007). Channel and perennial flow initiation in headwater streams: management implications of variability in source-area size. Environmental Management, 40(5), 775. https://doi.org/10.1007/s00267-005-0311-2.

Jaeger, K. L., Sando, R., McShane, R. R., Dunham, J. B., Hockman-Wert, D. P., Kaiser, K. E., ... & Blasch, K. W. (2019). Probability of Streamflow Permanence Model (PROSPER): A spatially continuous model of annual streamflow permanence throughout the Pacific Northwest. Journal of Hydrology X, 2, 100005. https://doi.org/10.1016/j.hydroa.2018.100005.

Jensen, C., McGuire, K., & Prince, P. (2017). Headwater stream length dynamics across four physiographic provinces of the Appalachian Highlands. Hydrological Processes, 31, 3350–3363. https://doi.org/10.1002/hyp.11259.

Jensen, C. K., McGuire, K. J., Shao, Y., & Andrew Dolloff, C. (2018). Modeling wet headwater stream networks across multiple flow conditions in the Appalachian Highlands. Earth Surface Processes and Landforms, 43(13), 2762-2778. https://doi.org/10.1002/esp.4431.

Jensen, C. K., McGuire, K. J., McLaughlin, D. L., & Scott, D. T. (2019). Quantifying spatiotemporal variation in headwater stream length using flow intermittency sensors. Environmental monitoring and assessment, 191(4), 226. https://doi.org/10.1007/s10661-019-7373-8.

Jenson, S.K., & Domingue, J.O. (1988). Extracting topographic structure from digital elevation data for geographic information system analysis. Photogrammetric Engineering and Remote Sensing, 54(11), 1593-1600. https://doi.org/0099-1112/88/5411-1593$02.25/0.

Kaplan, N. H., Sohrt, E., Blume, T., & Weiler, M. (2019). Monitoring ephemeral, intermittent and perennial streamflow: a dataset from 182 sites in the Attert catchment, Luxembourg. Earth System Science Data, 11, 1363-1374. https://doi.org/10.5194/essd-11-1363-2019.

Kim, S., & Sharma, A. (2019). The role of floodplain topography in deriving basin discharge using passive microwave remote sensing. Water Resources Research, 55(2), 1707-1716. https://doi.org/10.1029/2018WR023627.

Köppen, W. (1936). Das geographisca System der Klimate In: W. Köppen and G. Geiger, ed. Handbuch der Klimatologie (Handbuch der Klimatologie, vol. 1: C. Gebr, Borntraeger). http://koeppen-geiger.vu-wien.ac.at/pdf/Koppen_1936.pdf.

Larned S.T., Datry T., Arscott D.B., Tockner K. (2010). Emerging concepts in temporary-river ecology. Freshwater Biology 5: 717–738. https://doi.org/10.1111/j.1365-2427.2009.02322.x.

Li J., Wong D.W. (2010). Effects of DEM sources on hydrologic applications. Computers, Environment and Urban Systems 34: 251–261. https://doi.org/10.1016/j.compenvurbsys.2009.11.002.

Lovill, S. M., Hahm, W. J., & Dietrich, W. E. (2018). Drainage from the critical zone: Lithologic controls on the persistency and spatial extent of wetted channels during the summer dry season. Water Resources Research, 54(8), 5702-5726. https://doi.org/10.1029/2017WR021903.

Malard, F., Uehlinger, U., Zah, R., & Tockner, K. (2006). Flood-pulse and riverscape dynamics in a braided glacial river. Ecology, 87(3), 704-716. https://doi.org/10.1890/04-0889.

McInerney, D., Kavetski, D., Thyer, M., Lerat, J., & Kuczera, G. (2019). Benefits of Explicit Treatment of Zero Flows in Probabilistic Hydrological Modeling of Ephemeral Catchments. Water Resources Research. https://doi.org/10.1029/2018WR024148.

Medici, C., Butturini, A., Bernal, S., Vázquez, E., Sabater, F., Vélez, J. I., & Francés, F. (2008). Modelling the non-linear hydrological behaviour of a small Mediterranean forested catchment. Hydrological Processes: An International Journal, 22(18), 3814-3828. https://doi.org/10.1002/hyp.6991.

Mendicino, G., & Sole, A. (1997). The information content theory for the estimation of the topographic index distribution used in TOPMODEL. Hydrological Processes, 11(9), 1099-1114. https://doi.org/10.1002/(SICI)1099-1085(199707)11:9<1099::AID-HYP547>3.0.CO;2-F.

Mendicino, G. (1999). Sensitivity analysis on GIS procedures for the estimate of soil erosion risk. Natural Hazards, 20(2-3), 231-253. https://doi.org/10.1023/A:1008120231103.

Mendicino, G., & Colosimo, F. (2019). Analysis of Flow Resistance Equations in Gravel-Bed Rivers With Intermittent Regimes: Calabrian fiumare Data Set. Water Resources Research, 55(8), 7294-7319. https://doi.org/10.1029/2019WR024819.

Mendicino, G., & Senatore, A. (2013a). Evaluation of parametric and statistical approaches for the regionalization of flow duration curves in intermittent regimes. Journal of hydrology, 480, 19-32. https://doi.org/10.1016/j.jhydrol.2012.12.017.

Mendicino, G., & Senatore, A. (2013b). Regionalization of the Hargreaves Coefficient for the Assessment of Distributed Reference Evapotranspiration in Southern Italy. Journal of Irrigation and Drainage Engineering, 139(5), pp. 349–362, doi: 10.1061/(ASCE)IR.1943-4774.0000547.

Morgan, R. (1972). Observations on factors affecting the behaviour of a first-order stream. Transactions of the Institute of British Geographers, 56, 171–185. DOI: 10.2307/621547. https://www.jstor.org/stable/621547.

Nikolaidis, N. P., Demetropoulou, L., Froebrich, J., Jacobs, C., Gallart, F., Prat, N., ... & Davy, T. (2013). Towards sustainable management of Mediterranean river basins: policy recommendations on management aspects of temporary streams. Water Policy, 15(5), 830-849. doi: https://doi.org/10.2166/wp.2013.158.

Paillex, A., Siebers, A. R., Ebi, C., Mesman, J., & Robinson, C. T. (2020). High stream intermittency in an alpine fluvial network: Val Roseg, Switzerland. Limnology and Oceanography, 65(3), 557-568. https://doi.org/10.1002/lno.11324.

Payn, R. A., Gooseff, M. N., McGlynn, B. L., Bencala, K. E., & Wondzell, S. M. (2012). Exploring changes in the spatial distribution of stream baseflow generation during a seasonal recession. Water Resources Research, 48(4). https://doi.org/10.1029/2011WR011552.

Peirce, S. E., & Lindsay, J. B. (2015). Characterizing ephemeral streams in a southern Ontario watershed using electrical resistance sensors. Hydrological processes, 29(1), 103-111. https://doi.org/10.1002/hyp.10136.

945 Perez, A.B.A., Innocente dos Santos, C., Sá, J.H.M., Arienti, P.F., & Chaffe, P.L.B. (2020).
946 Connectivity of Ephemeral and Intermittent Streams in a Subtropical Atlantic Forest
947 Headwater Catchment. Water, 12, 1526. https://doi.org/10.3390/w12061526.

948 Phillips, R. W., Spence, C., & Pomeroy, J. W. (2011). Connectivity and runoff dynamics in
949 heterogeneous basins. Hydrological Processes, 25(19), 3061-3075.
950 https://doi.org/10.1002/hyp.8123.

951 Prancevic, J. P., & Kirchner, J. W. (2019). Topographic controls on the extension and retraction
952 of flowing streams. Geophysical Research Letters, 46(4), 2084-2092.
953 https://doi.org/10.1029/2018GL081799.

954 Reyjol, Y., Argillier, C., Bonne, W., Borja, A., Buijse, A. D., Cardoso, A. C., ... & Prat, N.
955 (2014). Assessing the ecological status in the context of the European Water Framework
956 Directive: where do we go now? Science of the Total Environment, 497, 332-344.
957 https://doi.org/10.1016/j.scitotenv.2014.07.119

958 Roberts, M. C., & Archibold, O. W. (1978). Variation of drainage density in a small british
959 columbia watershed 1. JAWRA Journal of the American Water Resources Association,
960 14(2), 470-476. https://doi.org/10.1111/j.1752-1688.1978.tb02183.x.

961 Schiller, D. V., Marcé, R., Obrador, B., Gómez-Gener, L., Casas-Ruiz, J. P., Acuña, V., &
962 Koschorreck, M. (2014). Carbon dioxide emissions from dry watercourses. Inland waters,
963 4(4), 377-382. https://doi.org/10.5268/IW-4.4.746.

964 Senatore, A., Mendicino, G., Smiatek, G., & Kunstmann, H. (2011). Regional climate change
965 projections and hydrological impact analysis for a Mediterranean basin in Southern Italy.
966 Journal of Hydrology, 399(1-2), 70-92. https://doi.org/10.1016/j.jhydrol.2010.12.035.

967 Senatore, A., Micieli, M., Liotti, A., Durighetto, N., Mendicino, G, & Botter, G. (2020).
968 Monitoring and modeling drainage network contraction and dry down in Mediterranean
969 Headwater catchments [data collection]. Retrieved from
970 http://researchdata.cab.unipd.it/id/eprint/375 doi:
971 10.25430/researchdata.cab.unipd.it.00000375

972 Shaw, S. B. (2016). Investigating the linkage between streamflow recession rates and channel
973 network contraction in a mesoscale catchment in New York state. Hydrological
974 Processes, 30(3), 479-492. https://doi.org/10.1002/hyp.10626.

975 Shaw, S. B., Bonville, D. B., & Chandler, D. G. (2017). Combining observations of channel
976 network contraction and spatial discharge variation to inform spatial controls on baseflow
977 in Birch Creek, Catskill Mountains, USA. Journal of Hydrology: Regional Studies, 12, 1-
978 12. https://doi.org/10.1016/j.ejrh.2017.03.003.

979 Skoulikidis, N. T., Sabater, S., Datry, T., Morais, M. M., Buffagni, A., Dörflinger, G., ... &
980 Rosado, J. (2017). Non-perennial Mediterranean rivers in Europe: status, pressures, and
981 challenges for research and management. Science of the Total Environment, 577, 1-18.
982 https://doi.org/10.1016/j.scitotenv.2016.10.147.

983 Spence, C., & Mengistu, S. (2016). Deployment of an unmanned aerial system to assist in
984 mapping an intermittent stream. Hydrological Processes, 30(3), 493-500.
985 https://doi.org/10.1002/hyp.10597.

Tomaštík, J., Mokroš, M., Surový, P., Grznárová, A., & Merganič, J. (2019). UAV RTK/PPK Method—An Optimal Solution for Mapping Inaccessible Forested Areas?. Remote sensing, 11(6), 721. https://doi.org/10.3390/rs11060721.

Tooth, S. (2000). Process, form and change in dryland rivers: A review of recent research. Earth-Science Reviews 5: 67–107. https://doi.org/10.1016/S0012-8252(00)00014-3.

Tortorici, L., Monaco, C., Tansi, C., Cocina, O. (1995). Recent and active tectonics in the Calabrian Arc (south Italy). Tectonophysics 243:37–55.

Van Meerveld, H. J., Kirchner, J. W., Vis, M. J., Assendelft, R. S., & Seibert, J. (2019). Expansion and contraction of the flowing stream network alter hillslope flowpath lengths and the shape of the travel time distribution. Hydrology and Earth System Sciences, 23(11), 4825-4834. https://doi.org/10.5194/hess-23-4825-2019.

Vander Vorste, R., Sarremejane, R., & Datry, T. (2019). Intermittent Rivers and Ephemeral Streams: A Unique Biome With Important Contributions to Biodiversity and Ecosystem Services. In: Reference Module in Earth Systems and Environmental Sciences, Elsevier. https://doi.org/10.1016/B978-0-12-409548-9.12054-8.

Ward, A. S., Schmadel, N. M., & Wondzell, S. M. (2018). Simulation of dynamic expansion, contraction, and connectivity in a mountain stream network. Advances in Water Resources, 114, 64-82. https://doi.org/10.1016/j.advwatres.2018.01.018.

Ward, A. S., Wondzell, S. M., Schmadel, N.M., & Herzog, S.P. (2020). Climate Change Causes River Network Contraction and Disconnection in the H.J. Andrews Experimental Forest, Oregon, USA. Front. Water 2:7. doi: 10.3389/frwa.2020.00007.

Whiting, J. A., & Godsey, S. E. (2016). Discontinuous headwater stream networks with stable flowheads, Salmon River basin, Idaho. Hydrological Processes, 30(13), 2305-2316. https://doi.org/10.1002/hyp.10790.

Wigington Jr, P. J., Moser, T. J., & Lindeman, D. R. (2005). Stream network expansion: a riparian water quality factor. Hydrological Processes: An International Journal, 19(8), 1715-1721. https://doi.org/10.1002/hyp.5866.

Zehe, E., & Sivapalan, M. (2009). Threshold behaviour in hydrological systems as (human) geo-ecosystems: Manifestations, controls, implications. Hydrol. Earth Syst. Sci., 13, 1273-1297.

Zimmer, M. A., & McGlynn, B. L. (2017). Ephemeral and intermittent runoff generation processes in a low relief, highly weathered catchment. Water Resources Research, 53(8), 7055-7077. https://doi.org/10.1002/2016WR019742.

Zimmer, M. A., & McGlynn, B. L. (2018). Lateral, vertical, and longitudinal source area connectivity drive runoff and carbon export across watershed scales. Water Resources Research, 54(3), 1576-1598. https://doi.org/10.1002/2017WR021718.

Zimmer, M. A., Kaiser, K. E., Blaszczak, J. R., Zipper, S. C., Hammond, J. C., Fritz, K. M., Costigan, K. H., Hosen, J., Godsey, S. E., Allen, G. H., et al. (2020). Zero or not? Causes and consequences of zero-flow stream gage readings. WIREs Water, 7(3), e1436.